Journal of Computational Physics 227 (2008) 10018–10039

Contents lists available at ScienceDirect

Journal of Computational Physics

journal homepage: www.elsevier.com/locate/jcp

A CG-FFT approach to the solution of a stress-velocity formulation of three-dimensional elastic scattering problems

Jiaqi Yang [a,*], Aria Abubakar [b], Peter M. van den Berg [c], Tarek M. Habashy [b], Fernando Reitich [a]

[a] University of Minnesota, School of Mathematics, 206 Church Street SE, 127 Vincent Hall, Minneapolis, MN 55455, USA
[b] Schlumberger-Doll Research, Cambridge, USA
[c] Delft University of Technology, Delft, The Netherlands

ARTICLE INFO

Article history:
Received 3 November 2007
Received in revised form 1 July 2008
Accepted 31 July 2008
Available online 23 August 2008

Keywords:
Elastic
3-D
CG-FFT
Integral equation

ABSTRACT

In this paper we introduce a Conjugate Gradient Fast Fourier Transform (CG-FFT) scheme for the numerical solution of the integral equation formulating three-dimensional elastic scattering problems. The formulation is in terms of the stress tensor and particle velocities as the unknown field variables. In contrast with the formulation based on particle displacements, this approach leads to integral representations that do not involve derivatives of the unknown fields, thus resulting in simplified and more stable numerics. The numerical procedure is based on suitable quadrature formulas that provide (second order) accurate approximations while retaining the convolution nature of the relevant integrals that make them amenable to efficient evaluation via FFTs. The scheme is further improved through the introduction of (approximation-based) pre-conditioners that are shown to accelerate the convergence of the CG iterations. Numerical results are presented that demonstrate the accuracy and efficiency of the proposed methodology.

1. Introduction

Elastic wave propagation plays an important role in a variety of engineering and industrial processes, ranging from geophysical prospecting [14,13] and non-destructive testing [32,27] to imaging applications in medicine [18,31]. The ability to accurately and efficiently simulate elastic wave scattering processes has therefore acquired great relevance, as it can significantly accelerate the improvement of existing technologies as well as the development of new ones. A testament to this is provided by the vast literature that has dealt with the development of numerical algorithms for the solution of elastic scattering problems and which has resulted in advanced methodologies based on finite elements (see e.g. [17] and the references therein), finite volumes, finite differences [23], and integral equations [5,10].

In this paper, we introduce a new approach to the simulation of (time-harmonic) elastic wave propagation that is based on an integral equation formulation. Our choice for an integral equation methodology is largely based on its recognized advantages over alternative formulations, particularly in inherently incorporating the radiation condition (which obviates the need for artificial absorbing boundaries) and their amenability to accelerated evaluation.

A number of related procedures have been proposed in the past, including some based on boundary-integral representations (suitable for piecewise homogeneous configurations, see e.g. [15,16,21,22]) as well as fully volumetric treatments (applicable to generally graded materials, e.g. [5–7]. The scheme we propose here falls under the latter category, as it seeks to solve a volumetric Lippman–Schwinger equation governing the elastic scattering problem. In contrast with previous work, we choose to formulate the equations in terms of the stress tensor and particle velocities [9] rather than viewing the particle

* Corresponding author.
E-mail address: yang0940@umn.edu (J. Yang).

0021-9991/$ - see front matter © 2008 Elsevier Inc. All rights reserved.
doi:10.1016/j.jcp.2008.07.027

displacements as the primitive variables. As we show, this approach leads to integral representations that do not involve spatial derivatives of the unknown fields, thus resulting in simplified and more stable numerics. Moreover, this stress-velocity formulation allows one to implement advanced approximation-based solutions such as the extended Born approximation [8] in a simple manner. Note that it is also possible to use the stress–displacement formulation instead of the stress-velocity formulation. The two formulations are equivalent since their relation is a simple algebraic one.

Beyond these characteristics, our numerical implementation includes a careful treatment of singular quadratures and of accelerated evaluations and it also incorporates suitable preconditioning schemes. In more detail, the accuracy of our method relies on the use of specialized quadrature formulas, based on averaging ("weakening") the Green function in the neighborhood of a singularity [26,29], which we show to result in second order accurate evaluations. As for acceleration, we resort to an iterative (conjugate gradient) procedure (CGNR [20] and BiCGStab [30]) to solve the discretized linear system where each iteration is effected via Fast Fourier Transforms. This so-called CG-FFT technique has also been used in the electromagnetic scattering computation both in the medical and geophysical applications [12,1,33,3]. Finally, to attain a further reduction of the overall computational effort, we investigate the effectiveness of pre-conditioners based on physical approximation, including the Born [24] and Extended Born approximations [4,8] and we show that application of the latter can deliver significant gains. As we demonstrate, the combination of this collection of techniques results in an efficient and accurate solver that could provide the basis for inversion procedures that require the repeated application of forward scattering simulators.

The rest of the paper is organized as follows: first, in Section 2, we describe the formulation of the scattering problem and set up the notation used in this paper. Section 3 is devoted to the derivation of the integral equations and to their normalization. In Section 4 we provide details on our approach to the numerical approximation of these equations, including a discussion of the "weakening" (averaging) procedure that we use to deal with the singular nature of the integrals. In this section we also describe the iterative methods we implemented to solve the discretized equations as well as present a review of approximate solutions (diagonalized, Born, extended Born) in connection with their use as pre-conditioners. Section 5 contains a number of numerical results that demonstrate the accuracy and efficiency of the proposed approach. And, finally, our conclusions are summarized in Section 6.

2. Scattering problem and governing equations

In an isotropic, linear and instantaneously reacting solid background D we consider the scattering of waves generated by the presence of inhomogeneities forming a subdomain B. The scatterer B is elastodynamically irradiated by given sources located in the embedding, see Fig. 1. The problem is to determine the total elastic wavefield in the given configuration.

Following the elastic wave theory and the notations in [9], the elastic wave motion in the frequency domain with time factor $\exp(st)$ is written as

$$-\Delta_{k,m,p,q}\partial_m\tau_{p,q} + s\rho v_k = f_k, \tag{1}$$

$$\Delta_{i,j,m,r}\partial_m v_r - sS_{i,j,p,q}\tau_{p,q} = h_{i,j}, \tag{2}$$

where ∂_m is the partial differential operator, $\tau_{p,q}$ is the stress tensor, v_k is the particle velocity, ρ is the mass density and $S_{i,j,p,q}$ is the compliance tensor written as

$$S_{i,j,p,q} = 3\Lambda\Delta^{\delta}_{i,j,p,q} + 2M\Delta_{i,j,p,q}, \tag{3}$$

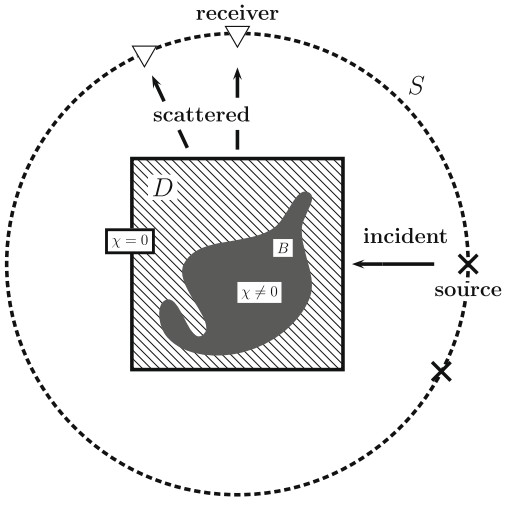

Fig. 1. The scattering experiment configuration.

in which $\Delta^{\delta}_{i,j,p,q}$ and $\Delta_{i,j,p,q}$ are unit tensors of rank four and defined as

$$\Delta^{\delta}_{i,j,p,q} = \frac{1}{3}\delta_{i,j}\delta_{p,q}, \quad \Delta_{i,j,p,q} = \frac{1}{2}(\delta_{i,p}\delta_{j,q} + \delta_{i,q}\delta_{j,p}). \tag{4}$$

On the right hand side of the governing equations, Eqs. (1) and (2), f_k is the force source and $h_{i,j}$ is the deformation rate source. All the subscripts can take on values of 1, 2 or 3, and they follow the so-called "summation convention" rule. Note that the tensors in Eq. (4) have the following properties:

$$\Delta^{\delta}_{i,j,p,q}\Delta^{\delta}_{p,q,k,l} = \Delta^{\delta}_{i,j,k,l}, \tag{5}$$

$$\Delta_{i,j,p,q}\Delta_{p,q,k,l} = \Delta_{i,j,k,l}, \tag{6}$$

$$\Delta^{\delta}_{i,j,p,q}\Delta_{p,q,k,l} = \Delta^{\delta}_{i,j,k,l}. \tag{7}$$

For contracted subscripts we note that $\Delta^{\delta}_{i,j,p,p} = \Delta_{i,j,p,p} = \delta_{i,j}$, where $\delta_{i,j}$ is Kronecker's unit tensor of rank two. The parameters Λ and M are related to the Lamé coefficients λ and μ as follows:

$$\lambda = \frac{-\Lambda}{2M(3\Lambda + 2M)}, \quad \mu = \frac{1}{4M}, \tag{8}$$

$$\Lambda = \frac{-\lambda}{2\mu(3\lambda + 2\mu)}, \quad M = \frac{1}{4\mu}. \tag{9}$$

Moreover, in this study, we choose to work with the particle velocity vector v_r instead of the displacement vector U_r. The relation between these two vectors are given by,

$$v_r = sU_r. \tag{10}$$

The stress and the velocity are the fundamental unknowns in our problem at hand. Alternatively, with Eq. (10) we can consider the stress and the displacement as fundamental unknowns as well. This does not change the equations fundamentally. However, we do not express the stress in terms of the particle velocity (or displacement) and we do not consider the particle velocity (or displacement) as fundamental unknowns.

In the scattering problem, the elastodynamic properties of the embedding are characterized by the material quantities ρ, Λ and M, and the elastodynamic properties of the scatterer are characterized by the material quantities $\rho^{\mathrm{sct}}(\boldsymbol{x})$, $\Lambda^{\mathrm{sct}}(\boldsymbol{x})$ and $M^{\mathrm{sct}}(\boldsymbol{x})$, where $\boldsymbol{x} = (x_1, x_2, x_3)$ is the three-dimensional (3D) spatial position vector in Cartesian coordinate. Therefore, we are interested in solving Eqs. (1) and (2) for wavefield $\{\tau_{p,q}, v_r\}$ when the sources $\{f_k, h_{i,j}\}$, the material properties $\{\rho, \Lambda, M\}$ and $\{\rho^{\mathrm{sct}}(\boldsymbol{x}), \Lambda^{\mathrm{sct}}(\boldsymbol{x}), M^{\mathrm{sct}}(\boldsymbol{x})\}$ are given.

3. Formulation of field integral equations

3.1. Expressions of the incident wavefields

In the integral equation approach, the standard procedure is to calculate first the so-called incident elastic wavefield, $\left\{\tau^{\mathrm{inc}}_{p,q}, v^{\mathrm{inc}}_r\right\}$, i.e. the wavefield that would be present in the configuration if the object shows no contrast with respect to its embedding ($\rho^{\mathrm{sct}}(\boldsymbol{x}) = \rho$, $\Lambda^{\mathrm{sct}}(\boldsymbol{x}) = \Lambda$ and $M^{\mathrm{sct}}(\boldsymbol{x}) = M$). Theoretically, the incident wavefield can be obtained through the following relations [9]:

$$-\tau^{\mathrm{inc}}_{p,q}(\boldsymbol{x}) = \int \left[G^{\tau,h}_{p,q,i,j}(\boldsymbol{x} - \boldsymbol{x}')h_{i,j}(\boldsymbol{x}') + G^{\tau,f}_{p,q,k}(\boldsymbol{x} - \boldsymbol{x}')f_k(\boldsymbol{x}')\right]\mathrm{d}\boldsymbol{x}', \tag{11}$$

$$v^{\mathrm{inc}}_r(\boldsymbol{x}) = \int \left[G^{v,h}_{r,i,j}(\boldsymbol{x} - \boldsymbol{x}')h_{i,j}(\boldsymbol{x}') + G^{v,f}_{r,k}(\boldsymbol{x} - \boldsymbol{x}')f_k(\boldsymbol{x}')\right]\mathrm{d}\boldsymbol{x}', \tag{12}$$

where the integration is over the domain that contains the sources, and where $G^{\tau,h}_{p,q,i,j}$ is the stress/deformation rate source Green function, $G^{\tau,f}_{p,q,k}$ is the stress/force source Green function, $G^{v,h}_{r,i,j}$ is the particle velocity/deformation rate source Green function and $G^{v,f}_{r,k}$ is the particle velocity/force source Green function. More precisely,

$$G^{\tau,h}_{p,q,i,j}(\boldsymbol{x}) = -\frac{1}{s}C_{p,q,i,j}\delta(\boldsymbol{x}) - \frac{1}{s\rho}C_{p,q,n,r}C_{k,m,i,j}\partial_n\partial_m G_{r,k}(\boldsymbol{x}, s), \tag{13}$$

$$G^{\tau,f}_{p,q,k}(\boldsymbol{x}) = \frac{1}{\rho}C_{p,q,n,r}\partial_n G_{r,k}(\boldsymbol{x}), \tag{14}$$

$$G^{v,h}_{r,i,j}(\boldsymbol{x}) = -\frac{1}{\rho}C_{k,m,i,j}\partial_m G_{r,k}(\boldsymbol{x}), \tag{15}$$

$$G^{v,f}_{r,k}(\boldsymbol{x}) = \frac{s}{\rho}G_{r,k}(\boldsymbol{x}), \tag{16}$$

and

$$G_{r,k}(\boldsymbol{x}) = \frac{1}{c_s^2}\delta_{r,k}G^s(\boldsymbol{x}) + \frac{1}{s^2}\partial_r\partial_k(G^p - G^s)(\boldsymbol{x}), \tag{17}$$

in which

$$G^p(\boldsymbol{x}) = \frac{\exp\left(-\frac{s}{c_p}|\boldsymbol{x}|\right)}{4\pi|\boldsymbol{x}|} \quad \text{and } G^s(\boldsymbol{x}) = \frac{\exp\left(-\frac{s}{c_s}|\boldsymbol{x}|\right)}{4\pi|\boldsymbol{x}|}, \tag{18}$$

are the Helmholtz Green functions [9]. Here $c_p = \sqrt{\frac{\lambda+2\mu}{\rho}}$ and $c_s = \sqrt{\frac{\mu}{\rho}}$ are the compressional wave speed and the shear wave speed of the embedding respectively. Further, $C_{i,j,p,q}$ is the stiffness tensor. In terms of the Lamé coefficients the stiffness tensor is given by

$$C_{i,j,p,q} = 3\lambda\Delta^{\delta}_{i,j,p,q} + 2\mu\Delta_{i,j,p,q} = \lambda\delta_{i,j}\delta_{p,q} + \mu(\delta_{i,p}\delta_{j,q} + \delta_{i,q}\delta_{j,p}). \tag{19}$$

In particular, when we have a monochromatic point force source located at $\boldsymbol{x}^S$ and oriented in α-direction, i.e.

$$f_k(\boldsymbol{x}) = \delta(\boldsymbol{x} - \boldsymbol{x}^S)\delta_{k,\alpha} \quad \text{and} \quad h_{i,j}(\boldsymbol{x}) = 0, \tag{20}$$

the incident wave fields are given by

$$-\tau^{inc}_{p,q}(\boldsymbol{x}) = \int G^{\tau,f}_{p,q,k}(\boldsymbol{x} - \boldsymbol{x}')\delta(\boldsymbol{x}' - \boldsymbol{x}^S)\delta_{k,\alpha}\mathrm{d}\boldsymbol{x}' = G^{\tau,f}_{p,q,\alpha}(\boldsymbol{x} - \boldsymbol{x}^S), \tag{21}$$

$$v^{inc}_r(\boldsymbol{x}) = \int G^{v,f}_{r,k}(\boldsymbol{x} - \boldsymbol{x}')\delta(\boldsymbol{x}' - \boldsymbol{x}^S)\delta_{k,\alpha}\mathrm{d}\boldsymbol{x}' = G^{v,f}_{r,\alpha}(\boldsymbol{x} - \boldsymbol{x}^S). \tag{22}$$

These integral representations are also the basis for the representations of the scattered field in terms of secondary sources due to the presence of a scattering object.

3.2. Expressions of the scattered wavefields

Next the scattered wavefield is obtained as follows:

$$\tau^{sct}_{p,q} = \tau_{p,q} - \tau^{inc}_{p,q}, v^{sct}_r = v_r - v^{inc}_r, \tag{23}$$

and, through the idea of Lippman–Schwinger type integral equation [28], the problem of determining the scattered wavefield is reduced to calculating its equivalent contrast source distribution, whose common support will be the domain D occupied by the scatterer.

Since the contrasts in the medium properties vanish outside the scattering object, the scattered field can be written as follows:

$$-\tau^{sct}_{p,q}(\boldsymbol{x}) = \int_D \left[G^{\tau,h}_{p,q,i,j}(\boldsymbol{x} - \boldsymbol{x}')h^{sct}_{i,j}(\boldsymbol{x}') + G^{\tau,f}_{p,q,k}(\boldsymbol{x} - \boldsymbol{x}')f^{sct}_k(\boldsymbol{x}')\right]\mathrm{d}\boldsymbol{x}', \tag{24}$$

$$v^{sct}_r(\boldsymbol{x}) = \int_D \left[G^{v,h}_{r,i,j}(\boldsymbol{x} - \boldsymbol{x}')h^{sct}_{i,j}(\boldsymbol{x}') + G^{v,f}_{r,k}(\boldsymbol{x} - \boldsymbol{x}')f^{sct}_k(\boldsymbol{x}')\right]\mathrm{d}\boldsymbol{x}', \tag{25}$$

The contrast sources $h^{sct}_{i,j}(\boldsymbol{x})$ and $f^{sct}_k(\boldsymbol{x})$ may be expressed in terms of the total wavefields through

$$h^{sct}_{i,j}(\boldsymbol{x}) = s\left[S^{sct}_{i,j,p,q}(\boldsymbol{x}) - S_{i,j,p,q}\right]\tau_{p,q}(\boldsymbol{x}) = s\Lambda\chi^{\Lambda}(\boldsymbol{x})\delta_{i,j}\tau_{k,k}(\boldsymbol{x}) + sM\chi^{M}(\boldsymbol{x})\left[\tau_{i,j}(\boldsymbol{x}) + \tau_{j,i}(\boldsymbol{x})\right], \tag{26}$$

$$f^{sct}_k(\boldsymbol{x}) = -s\rho\chi^{\rho}(\boldsymbol{x})v_k(\boldsymbol{x}), \tag{27}$$

where the three contrast quantities χ^{ρ}, χ^{Λ} and χ^{M} are given by

$$\chi^{\Lambda}(\boldsymbol{x}) = \frac{\Lambda^{sct}(\boldsymbol{x})}{\Lambda} - 1, \quad \chi^{M}(\boldsymbol{x}) = \frac{M^{sct}(\boldsymbol{x})}{M} - 1, \quad \chi^{\rho}(\boldsymbol{x}) = \frac{\rho^{sct}(\boldsymbol{x})}{\rho} - 1. \tag{28}$$

We finally note that, once the contrast sources $f^{sct}_k(\boldsymbol{x})$ and $h^{sct}_{i,j}(\boldsymbol{x})$ are known, the scattered field may be calculated using the source-type of integral representations of Eqs. (24) and (25).

3.3. Equations inside the computational domain

The total wavefield inside the object is determined from the Eqs. (24) and (25), by letting the point of observation to be inside the test domain D. We then obtain the system of integral equations

$$\tau^{\mathrm{inc}}_{p,q}(\boldsymbol{x}) = \tau_{p,q}(\boldsymbol{x}) + s\int_D \left[G^{\tau,h}_{p,q,i,i}\Lambda\chi^{\Lambda}(\boldsymbol{x}')\tau_{k,k}(\boldsymbol{x}') + G^{\tau,h}_{p,q,i,j}2M\chi^{M}(\boldsymbol{x}')\tau_{i,j}(\boldsymbol{x}') - G^{\tau,f}_{p,q,k}\rho\chi^{\rho}(\boldsymbol{x}')v_k(\boldsymbol{x}')\right]\mathrm{d}\boldsymbol{x}', \tag{29}$$

$$v^{\mathrm{inc}}_{r}(\boldsymbol{x}) = v_r(\boldsymbol{x}) - s\int_D \left[G^{v,h}_{r,i,i}\Lambda\chi^{\Lambda}(\boldsymbol{x}')\tau_{k,k}(\boldsymbol{x}') + G^{v,h}_{r,i,j}2M\chi^{M}(\boldsymbol{x}')\tau_{i,j}(\boldsymbol{x}') - G^{v,f}_{r,k}\rho\chi^{\rho}(\boldsymbol{x}')v_k(\boldsymbol{x}')\right]\mathrm{d}\boldsymbol{x}', \tag{30}$$

for $\boldsymbol{x}\in D$. Eqs. (29) and (30) form a system of integral equations for the six unknown components of the symmetric stress tensor $\tau_{p,q}$ and the three components of the particle velocity vector v_r. Note that in these integral equations the Green functions are spatially dependent on $\boldsymbol{x}-\boldsymbol{x}'$, i.e. $G^{\cdot\cdot}_{\cdot\cdot\cdot\cdot} = G^{\cdot\cdot}_{\cdot\cdot\cdot\cdot}(\boldsymbol{x}-\boldsymbol{x}')$. This convolution type of structure will be exploited.

3.4. Normalized field integral equations

To avoid any ill-conditioning that could arise as a result of the difference in magnitudes between the stress tensor and the particle velocity, we normalize the latter using the S-wave impedance $Z_s = \rho c_s$ and we propose to work with the re-normalized equations. More precisely, letting

$$u_r = Z_s v_r, \tag{31}$$

straightforward manipulations lead to the normalized equations:

$$\begin{aligned}\tau^{\mathrm{inc}}_{p,q}(\boldsymbol{x}) = \tau_{p,q}(\boldsymbol{x}) &+ s\Lambda\int_D G^{\tau,h}_{p,q,i,i}(\boldsymbol{x}-\boldsymbol{x}')\chi^{\Lambda}(\boldsymbol{x}')\tau_{k,k}(\boldsymbol{x}')\mathrm{d}\boldsymbol{x}' + 2sM\int_D G^{\tau,h}_{p,q,i,j}(\boldsymbol{x}-\boldsymbol{x}')\chi^{M}(\boldsymbol{x}')\tau_{i,j}(\boldsymbol{x}')\mathrm{d}\boldsymbol{x}'\\ &- \frac{s}{c_s}\int_D G^{\tau,f}_{p,q,k}(\boldsymbol{x}-\boldsymbol{x}')\chi^{\rho}(\boldsymbol{x}')u_k(\boldsymbol{x}')\mathrm{d}\boldsymbol{x}' = \tau_{p,q}(\boldsymbol{x}) + B^{\tau,\Lambda}_{p,q}(\boldsymbol{x}) + B^{\tau,M}_{p,q}(\boldsymbol{x}) + B^{\tau,\rho}_{p,q}(\boldsymbol{x}),\end{aligned} \tag{32}$$

$$\begin{aligned}\rho c_s v^{\mathrm{inc}}_{r}(\boldsymbol{x}) = u_r(\boldsymbol{x}) &- \rho c_s s\Lambda\int_D G^{v,h}_{r,i,i}(\boldsymbol{x}-\boldsymbol{x}')\chi^{\Lambda}(\boldsymbol{x}')\tau_{k,k}(\boldsymbol{x}')\mathrm{d}\boldsymbol{x}' - 2\rho c_s sM\int_D G^{v,h}_{r,i,j}(\boldsymbol{x}-\boldsymbol{x}')\chi^{M}(\boldsymbol{x}')\tau_{i,j}(\boldsymbol{x}')\mathrm{d}\boldsymbol{x}'\\ &+ s\rho\int_D G^{v,f}_{r,k}(\boldsymbol{x}-\boldsymbol{x}')\chi^{\rho}(\boldsymbol{x}')u_k(\boldsymbol{x}')\mathrm{d}\boldsymbol{x}' = u_r(\boldsymbol{x}) + B^{u,\Lambda}_{r}(\boldsymbol{x}) + B^{u,M}_{r}(\boldsymbol{x}) + B^{u,\rho}_{r}(\boldsymbol{x}),\end{aligned} \tag{33}$$

where, omitting the spatial dependence,

$$B^{\tau,\Lambda}_{p,q} = \frac{\lambda}{2\mu}\left[\delta_{p,q}\left(\frac{2c_s^2}{c_p^2}\chi^{\Lambda}\tau_{k,k} + \frac{\lambda s^2}{\rho c_p^4}A^{p,\Lambda}_{k,k}\right) + \frac{2c_s^2}{c_p^2}\partial_p\partial_q A^{p,\Lambda}_{k,k}\right], \tag{34}$$

$$\begin{aligned}B^{\tau,M}_{p,q} = &-\frac{\lambda}{2\mu}\left[\delta_{p,q}\left(\frac{2c_s^2}{c_p^2}\chi^{M}\tau_{k,k} + \frac{\lambda s^2}{\rho c_p^4}A^{p,M}_{k,k} + \frac{2c_s^2}{c_p^2}\partial_i\partial_j A^{p,M}_{i,j}\right) + \frac{2c_s^2}{c_p^2}\partial_p\partial_q A^{p,M}_{k,k}\right] - \chi^{M}\tau_{p,q} - \left(\partial_p\partial_j A^{s,M}_{j,q} + \partial_q\partial_j A^{s,M}_{j,p}\right)\\ &- \frac{2c_s^2}{s^2}\partial_p\partial_q\partial_i\partial_j\left(A^{p,M}_{i,j} - A^{s,M}_{i,j}\right),\end{aligned} \tag{35}$$

$$B^{\tau,\rho}_{p,q} = -\frac{\lambda}{\rho c_p^2}\frac{s}{c_s}\delta_{p,q}\partial_k A^{p,\rho}_{k} - \frac{s}{c_s}\left(\partial_p A^{s,\rho}_{q} + \partial_q A^{s,\rho}_{p}\right) - \frac{2\mu}{s\rho c_s}\partial_p\partial_q\partial_k(A^{p,\rho}_{k} - A^{s,\rho}_{k}), \tag{36}$$

$$B^{u,\Lambda}_{r} = -\frac{\lambda s c_s}{2\mu c_p^2}\partial_r A^{p,\Lambda}_{k,k}, \tag{37}$$

$$B^{u,M}_{r} = \frac{\lambda s c_s}{2\mu c_p^2}\partial_r A^{p,M}_{k,k} + \frac{s\rho c_s}{\mu}\partial_i A^{s,M}_{r,i} + \frac{c_s}{s}\partial_r\partial_i\partial_j\left(A^{p,M}_{i,j} - A^{s,M}_{i,j}\right), \tag{38}$$

$$B^{u,\rho}_{r} = \frac{s^2}{c_s^2}A^{s,\rho}_{r} + \partial_r\partial_k\left(A^{p,\rho}_{k} - A^{s,\rho}_{k}\right). \tag{39}$$

Here, the vector potentials are given by the following expressions:

$$A^{\gamma,\beta}_{i,j}(\boldsymbol{x}) = \int_D G^{\gamma}(\boldsymbol{x}-\boldsymbol{x}')\chi^{\beta}(\boldsymbol{x}')\tau_{i,j}(\boldsymbol{x}')\mathrm{d}\boldsymbol{x}', \tag{40}$$

$$A^{\gamma,\rho}_{r}(\boldsymbol{x}) = \int_D G^{\gamma}(\boldsymbol{x}-\boldsymbol{x}')\chi^{\rho}(\boldsymbol{x}')u_r(\boldsymbol{x}')\mathrm{d}\boldsymbol{x}', \tag{41}$$

where $\gamma\in\{\mathrm{p},\mathrm{s}\}$ and $\beta\in\{\Lambda, M\}$.

3.5. Normalized field integral equations of the scattered wavefields

One variation of Eqs. (32) and (33) is to split the total fields on the right hand side into two parts: incident fields and scattered fields. Upon transferring every term that involves the incident wavefields to the left hand side, we obtain

$$\tau^{\mathrm{prm}}_{p,q}(\boldsymbol{x}) = \tau^{\mathrm{sct}}_{p,q}(\boldsymbol{x}) + s\Lambda\int_D G^{\tau,h}_{p,q,i,i}(\boldsymbol{x}-\boldsymbol{x}')\chi^{\Lambda}(\boldsymbol{x}')\tau^{\mathrm{sct}}_{k,k}(\boldsymbol{x}')\mathrm{d}\boldsymbol{x}' + 2sM\int_D G^{\tau,h}_{p,q,i,j}(\boldsymbol{x}-\boldsymbol{x}')\chi^{M}(\boldsymbol{x}')\tau^{\mathrm{sct}}_{i,j}(\boldsymbol{x}')\mathrm{d}\boldsymbol{x}' - \frac{s}{c_{\mathrm{s}}}\int_D G^{\tau,f}_{p,q,k}(\boldsymbol{x}-\boldsymbol{x}')\chi^{\rho}(\boldsymbol{x}')u^{\mathrm{sct}}_k(\boldsymbol{x}')\mathrm{d}\boldsymbol{x}', \tag{42}$$

$$u^{\mathrm{prm}}_r(\boldsymbol{x}) = u^{\mathrm{sct}}_r(\boldsymbol{x}) - \rho c_{\mathrm{s}} s\Lambda\int_D G^{v,h}_{r,i,i}(\boldsymbol{x}-\boldsymbol{x}')\chi^{\Lambda}(\boldsymbol{x}')\tau^{\mathrm{sct}}_{k,k}(\boldsymbol{x}')\mathrm{d}\boldsymbol{x}' - 2\rho c_{\mathrm{s}} sM\int_D G^{v,h}_{r,i,j}(\boldsymbol{x}-\boldsymbol{x}')\chi^{M}(\boldsymbol{x}')\tau^{\mathrm{sct}}_{i,j}(\boldsymbol{x}')\mathrm{d}\boldsymbol{x}' + s\rho\int_D G^{v,f}_{r,k}(\boldsymbol{x}-\boldsymbol{x}')\chi^{\rho}(\boldsymbol{x}')u^{\mathrm{sct}}_k(\boldsymbol{x}')\mathrm{d}\boldsymbol{x}'. \tag{43}$$

where

$$\tau^{\mathrm{prm}}_{p,q}(\boldsymbol{x}) = -s\Lambda\int_D G^{\tau,h}_{p,q,i,i}(\boldsymbol{x}-\boldsymbol{x}')\chi^{\Lambda}(\boldsymbol{x}')\tau^{\mathrm{inc}}_{k,k}(\boldsymbol{x}')\mathrm{d}\boldsymbol{x}' - 2sM\int_D G^{\tau,h}_{p,q,i,j}(\boldsymbol{x}-\boldsymbol{x}')\chi^{M}(\boldsymbol{x}')\tau^{\mathrm{inc}}_{i,j}(\boldsymbol{x}')\mathrm{d}\boldsymbol{x}' + \frac{s}{c_{\mathrm{s}}}\int_D G^{\tau,f}_{p,q,k}(\boldsymbol{x}-\boldsymbol{x}')\chi^{\rho}(\boldsymbol{x}')u^{\mathrm{inc}}_k(\boldsymbol{x}')\mathrm{d}\boldsymbol{x}', \tag{44}$$

$$u^{\mathrm{prm}}_r(\boldsymbol{x}) = \rho c_{\mathrm{s}} s\Lambda\int_D G^{v,h}_{r,i,i}(\boldsymbol{x}-\boldsymbol{x}')\chi^{\Lambda}(\boldsymbol{x}')\tau^{\mathrm{inc}}_{k,k}(\boldsymbol{x}')\mathrm{d}\boldsymbol{x}' + 2\rho c_{\mathrm{s}} sM\int_D G^{v,h}_{r,i,j}(\boldsymbol{x}-\boldsymbol{x}')\chi^{M}(\boldsymbol{x}')\tau^{\mathrm{inc}}_{i,j}(\boldsymbol{x}')\mathrm{d}\boldsymbol{x}' - s\rho\int_D G^{v,f}_{r,k}(\boldsymbol{x}-\boldsymbol{x}')\chi^{\rho}(\boldsymbol{x}')u^{\mathrm{inc}}_k(\boldsymbol{x}')\mathrm{d}\boldsymbol{x}'. \tag{45}$$

Note that $\{\tau^{\mathrm{prm}}_{p,q}, u^{\mathrm{prm}}_r\}$ is the scattered field generated by the incident field in the scattering domain, in seismic often denoted as the primary field. Correction to this primary scattered field is obtained by solving for $\tau^{\mathrm{sct}}_{i,j}(\boldsymbol{x})$ and $u^{\mathrm{sct}}_k(\boldsymbol{x})$ from Eqs. (42) and (43). Subsequently, the total wavefields follow from the following relations:

$$\tau_{i,j}(\boldsymbol{x}) = \tau^{\mathrm{sct}}_{i,j}(\boldsymbol{x}) + \tau^{\mathrm{inc}}_{i,j}(\boldsymbol{x}), \quad u_k(\boldsymbol{x}) = u^{\mathrm{sct}}_k(\boldsymbol{x}) + u^{\mathrm{inc}}_k(\boldsymbol{x}), \quad \boldsymbol{x}\in D. \tag{46}$$

This special formulation (the so-called scattered field integral equation formulation) will be used to arrive at an improved extended Born approximation solution.

3.6. Scattered particle velocities at the receivers

After obtaining the stress tensor and the particle velocity vector inside the test domain D, from Eq. (30), the scattered field of the particle velocity at the receiver positions (i.e. $\boldsymbol{x}^R \notin D$) can be calculated as follows:

$$v^{\mathrm{sct}}_r(\boldsymbol{x}^R) = \frac{\lambda}{2\mu}\frac{s}{\rho c^2_{\mathrm{p}}}\int_D \partial_r G^{\mathrm{p}}\chi^{\Lambda}\tau_{k,k}\mathrm{d}\boldsymbol{x} - \frac{\lambda}{2\mu}\frac{s}{\rho c^2_{\mathrm{p}}}\int_D \partial_r G^{\mathrm{p}}\chi^{\mathrm{M}}\tau_{k,k}\mathrm{d}\boldsymbol{x} - \frac{1}{\rho s}\int_D \partial_r\partial_i\partial_j(G^{\mathrm{p}}-G^{\mathrm{s}})\chi^{\mathrm{M}}\tau_{i,j}\mathrm{d}\boldsymbol{x} - \frac{s}{\rho c^2_{\mathrm{s}}}\int_D \partial_j G^{\mathrm{s}}\chi^{M}\tau_{r,j}\mathrm{d}\boldsymbol{x} - \frac{s^2}{\rho c^3_{\mathrm{s}}}\int_D G^{\mathrm{s}}\chi^{\rho}u_r\mathrm{d}\boldsymbol{x} - \frac{1}{\rho c_{\mathrm{s}}}\int_D \partial_r\partial_k(G^{\mathrm{p}}-G^{\mathrm{s}})\chi^{\rho}u_k\mathrm{d}\boldsymbol{x}, \tag{47}$$

where we have omitted the spatial dependence of $\boldsymbol{x}^R - \boldsymbol{x}$ in the Green functions G^{p} and G^{s} and the spatial dependence $\boldsymbol{x}$ in the contrast functions χ^M,χ^{Λ} and χ^{ρ} as well as in the field functions $\tau_{i,j}$ and u_r. The partial derivatives operating on the Helmholtz Green function are calculated analytically, see [9].

4. Numerical treatment

4.1. Discretization procedure

We assume that the domain D which contains the scatterers is a rectangular domain with boundaries along the x_1-, x_2- and x_3-direction. A Cartesian coordinate system is centered in D. We discretize the domain D in a rectangular mesh. The mesh is uniformly spaced in the x_1-, x_2 and x_3-direction. The rectangular subdomains with widths Δx_1 in the x_1-direction, Δx_2 in the x_2-direction, and Δx_3 in the x_3-direction are given by

$$D_{m,n,l} = \left\{ (x_1,x_2,x_3)\in\mathcal{R}^3 \middle| \begin{array}{l} x_{1;m}-\frac{1}{2}\Delta x_1 < x_1 < x_{1;m}+\frac{1}{2}\Delta x_1 \\ x_{2;n}-\frac{1}{2}\Delta x_2 < x_2 < x_{2;n}+\frac{1}{2}\Delta x_2 \\ x_{3;l}-\frac{1}{2}\Delta x_3 < x_3 < x_{3;l}+\frac{1}{2}\Delta x_3 \end{array} \right\} \tag{48}$$

where

$$x_{1;m} = x_{1;1/2} + \left(m - \frac{1}{2}\right)\Delta x_1, \quad m = 1, \ldots, M, \tag{49}$$

$$x_{2;n} = x_{2;1/2} + \left(n - \frac{1}{2}\right)\Delta x_2, \quad n = 1, \ldots, N, \tag{50}$$

$$x_{3;l} = x_{3;1/2} + \left(l - \frac{1}{2}\right)\Delta x_3, \quad l = 1, \ldots, L, \tag{51}$$

in which $x_{1;1/2}$ is the lower x_1 bound of domain D, $x_{2;1/2}$ is its lower x_2 bound, and $x_{3,1/2}$ is its lower x_3 bound. In each subdomain $D_{m,n,l}$ with center points at $\boldsymbol{x}_{mnl} = (x_{1;m}, x_{2,n}, x_{3,l})$, we assume the material contrasts χ^{Λ}, χ^{M} and χ^{ρ} to be constant, with values chosen to be the same as their values at the center point

$$\chi^{\beta}_{m,n,l} = \chi^{\beta}(\boldsymbol{x}_{m,n,l}), \quad \text{where} \quad \beta \in \{\Lambda, M, \rho\}. \tag{52}$$

In view of the presence of spatial differentiations in the integral operators, the boundary of the domain D is chosen to lie completely outside the scattering objects, and hence

$$\chi^{\beta}_{1,n,l} = 0, \quad \chi^{\beta}_{M,n,l} = 0, \quad \forall n, \forall l, \tag{53}$$

$$\chi^{\beta}_{m,1,l} = 0, \quad \chi^{\beta}_{m,N,l} = 0, \quad \forall m, \forall l, \tag{54}$$

$$\chi^{\beta}_{m,n,1} = 0, \quad \chi^{\beta}_{m,n,L} = 0, \quad \forall m, \forall n. \tag{55}$$

Now using the spatial discretization grid described above, we are able to discretize the continuous quantities. For example, $\tau_{p,q;m,n,l}$ is defined

$$\tau_{p,q;m,n,l} = \tau_{p,q}(\boldsymbol{x}_{m,n,l}). \tag{56}$$

Therefore, Eqs. (32) and (33) are discretized as follows:

$$\tau^{inc}_{p,q;m,n,l} = \tau_{p,q;m,n,l} + B^{\tau,\Lambda}_{p,q;m,n,l} + B^{\tau,M}_{p,q;m,n,l} + B^{\tau,\rho}_{p,q;m,n,l}, \tag{57}$$

$$\rho c_s v^{inc}_{r;m,n,l} = u_{r;m,n,l} + B^{u,\Lambda}_{r;m,n,l} + B^{u,M}_{r;m,n,l} + B^{u,\rho}_{r;m,n,l}, \tag{58}$$

for $m = 1, \ldots, M$, $n = 1, \ldots, N$, and $l = 1, \ldots, L$.

4.2. Weakening procedure

Next, the continuous representation of the vector potentials in Eqs. (40) and (41) ought to be discretized in a similar way. However, in order to cope with the singularity of the Green function, we take the spherical mean of the normalized vector potential in the Cartesian space. We integrate each vector potential over a spherical domain [26,29] in the Cartesian space with center at the point $\boldsymbol{x}_{m,n,l} = (x_{1;m}, x_{2;n}, x_{3;l})$ with radius $\frac{1}{2}\Delta x = \frac{1}{2}\min(\Delta x_1, \Delta x_2, \Delta x_3)$. The results are divided by the volume of the spherical domain with radius $\frac{1}{2}\Delta x$. For instance,

$$A^{\mathrm{p},\Lambda}_{i,j}(\boldsymbol{x}_{m,n,l}) = \frac{\int_{|\boldsymbol{x}''|<1/2\Delta x} A^{\mathrm{p},\Lambda}_{i,j}(\boldsymbol{x}_{m,n,l} + \boldsymbol{x}'')\mathrm{d}\boldsymbol{x}''}{\int_{|\boldsymbol{x}''|<1/2\Delta x}\mathrm{d}\boldsymbol{x}''} = \int_D \mathcal{G}^{\mathrm{p}}(\boldsymbol{x}_{m,n,l} - \boldsymbol{x}')\chi^{\Lambda}(\boldsymbol{x}')\tau_{i,j}(\boldsymbol{x}')\mathrm{d}\boldsymbol{x}', \tag{59}$$

where we have interchanged the order of integrations, such that

$$\mathcal{G}^{\mathrm{p}}(\boldsymbol{x}) = \frac{\int_{|\boldsymbol{x}''|<1/2\Delta x} G^{\mathrm{p}}(\boldsymbol{x} + \boldsymbol{x}'')\mathrm{d}\boldsymbol{x}'}{\int_{|\boldsymbol{x}''|<\frac{1}{2}\Delta x}\mathrm{d}\boldsymbol{x}''} = \begin{cases} \dfrac{\left[1 + \frac{s}{2c_{\mathrm{p}}}\Delta x\right]\exp\left(-\frac{s}{2c_{\mathrm{p}}}\Delta x\right) - 1}{-\frac{s^2}{6c_{\mathrm{p}}^2}\pi\Delta x^3}, & R = 0, \\ \dfrac{\exp\left[-\frac{s}{c_{\mathrm{p}}}R\right]\left[\frac{\sinh\left(\frac{s}{2c_{\mathrm{p}}}\Delta x\right)}{\frac{s}{2c_{\mathrm{p}}}\Delta x} - \cosh\left(\frac{s}{2c_{\mathrm{p}}}\Delta x\right)\right]}{-\frac{s^2}{3c_{\mathrm{p}}^2}\pi\Delta x^2 R}, & R > \frac{1}{2}\Delta x, \end{cases} \tag{60}$$

in which $R = |\boldsymbol{x}| = \left(x_1^2 + x_2^2 + x_3^2\right)^{\frac{1}{2}}$ is the distance function.

As a result of this weakening procedure, we are now able to compute the integral over D in Eq. (59) numerically. We approximate the integral in Eq. (59) using a midpoint rule. We then arrive at the vector potential $A^{\mathrm{p},\Lambda}_{i,j;m,n,l} = A^{\mathrm{p},\Lambda}_{i,j}(\boldsymbol{x}_{m,n,l})$ given by

$$A^{\mathrm{p},\Lambda}_{i,j;m,n,l} = \Delta V \sum_{m'=1}^{M}\sum_{n'=1}^{N}\sum_{l'=1}^{L} \mathcal{G}^{\mathrm{p}}(\boldsymbol{x}_{m,n,l} - \boldsymbol{x}_{m',n',l'})\chi^{\Lambda}_{m',n',l'}\tau_{i,j;m',n',l'}, \tag{61}$$

for $m = -1, \ldots, M+2$, $n = -1, \ldots, N+2$, and $l = -1, \ldots, L+2$, where $\Delta V = \Delta x_1 \Delta x_2 \Delta x_3$ denotes the volume of each subdomain. Hence, following the above discretization procedure, all the vector potentials in Eqs. (40) and (41) are discretized into totally 19 convolutions in a similar form to Eq. (61). These convolutions can be calculated efficiently using an FFT routine, (see [25]).

From the considerations above it is straightforward to obtain complete expressions for the discretized form of equations Eqs. (57) and (58). For instance, for $B^{\tau,\Lambda}_{p,q;m,n,l}$ we have

$$B^{\tau,\Lambda}_{1,1;m,n,l}=\frac{\lambda}{\rho c_{\mathrm{p}}^2}\chi^{\Lambda}_{m,n,l}\tau_{k,k}+\frac{\lambda}{\rho c_{\mathrm{p}}^2}\frac{\lambda s^2}{2\mu c_{\mathrm{p}}^2}A^{\mathrm{p},\Lambda}_{k,k;m,n,l}+\frac{\lambda}{\rho c_{\mathrm{p}}^2}\frac{1}{(\Delta x_1)^2}\left(A^{\mathrm{p},\Lambda}_{k,k;m-1,n,l}-2A^{\mathrm{p},\Lambda}_{k,k;m,n,l}+A^{\mathrm{p},\Lambda}_{k,k;m+1,n,l}\right), \tag{62}$$

and similar representations can be obtained for the remaining components.

4.3. Linear equation solvers and pre-conditioners

Since the linear equation system of Eqs. (57) and (58) has $9\times M\times N\times L$ unknowns (for each source position/orientation and frequency) and the corresponding matrix is densely full, iterative linear equation solvers will be more suitable than direct solvers. However, among the various iterative linear equation solvers, the conjugate gradient techniques are more attractive for the problem at hand. By using these techniques, the matrix does not need to be stored, hence the memory cost is therefore minimized.

Since the matrix of operation here is not positive definite, we first choose to use the so-called CGNR method [19], due to its well-known versatility and stability. More precisely, the adjoint operator of the given linear operator is applied as a pre-conditioner in the scheme of pre-conditioned Conjugate Gradient method, so that the matrix of operation becomes positive definite. However, the condition number of the resulting linear operator is twice that of the original one, which makes the convergence rate slower. Hence, we propose to use its diagonal matrix as a pre-conditioner, which is shown to be helpful in the numerical tests.

Besides the CGNR technique, BiCGStab is another attractive iterative linear equation solver [30]. However it suffers from irregular convergence behavior when the matrix is ill-conditioned. To improve the performance of these linear equation solvers, we propose an alternative type of pre-conditioners: the extended Born approximation (EBA) [8] pre-conditioner.

4.3.1. Adjoint operator and its explicit expression

In order to implement the so-called CGNR linear equation solver, we first have to write out the explicit expression of its adjoint operator. The adjoint operators $\mathcal{K}^*$ is defined through the relation

$$\langle r_{p,q},\mathcal{K}s_{p,q}\rangle_D=\langle\mathcal{K}^*r_{p,q},s_{p,q}\rangle_D, \tag{63}$$

where $r_{p,q}$ and $s_{p,q}$ are both in the same tensor space, in domain D. Note that $s_{0,1}$, $s_{0,2}$ and $s_{0,3}$ are referred to u_1, u_2 and u_3, while other $s_{p,q}$'s are referred to the six components of $\tau_{p,q}$. The inner product on D is therefore defined as follows:

$$\langle a_{p,q},b_{p,q}\rangle_D=\sum_{(p,q)\in\Phi}\sum_{m=1}^{M}\sum_{n=1}^{N}\sum_{l=1}^{L}a_{p,q;m,n,l}\bar{b}_{p,q;m,n,l}, \tag{64}$$

where $\Phi=\{(1,1),(2,2),(3,3),(1,2),(1,3),(2,3),(0,1),(0,2),(0,3)\}$.

These definitions allow us to get the explicit expression of $\mathcal{K}^*$. Here we list only one component of $\mathcal{K}^*r_{p,q}$ as an illustration:

$$\begin{aligned}\left(\mathcal{K}^*r_{p,q}\right)_{1,1;m,n,l}=&\overline{\frac{\lambda}{\rho c_{\mathrm{p}}^2}}\overline{\chi^{\Lambda}_{m,n,l}}r_{k,k;m,n,l}-\overline{\chi^{M}_{m,n,l}}r_{1,1;m,n,l}-\overline{\left(\frac{\lambda}{\rho c_{\mathrm{p}}^2}\right)}\overline{\chi^{M}_{m,n,l}}r_{k,k;m,n,l}+\overline{\chi^{\Lambda}_{m,n,l}}\Delta V\sum_{m'=-1}^{M+2}\sum_{n'=-1}^{N+2}\sum_{l'=-1}^{L+2}\overline{\mathcal{G}^{\mathrm{s}}}(\boldsymbol{x}_{m,n,l}-\boldsymbol{x}_{m',n',l'})F^{\mathrm{p},\Lambda}_{m',n',l'}\\&-\overline{\chi^{M}_{m,n,l}}\Delta V\sum_{m'=-1}^{M+2}\sum_{n'=-1}^{N+2}\sum_{l'=-1}^{L+2}\overline{\mathcal{G}^{\mathrm{p}}}(\boldsymbol{x}_{m,n,l}-\boldsymbol{x}_{m',n',l'})F^{\mathrm{p},M}_{1,1;m',n',l'}-\overline{\chi^{M}_{m,n,l}}\Delta V\sum_{m'=-1}^{M+2}\sum_{n'=-1}^{N+2}\sum_{l'=-1}^{L+2}\overline{\mathcal{G}^{\mathrm{s}}}(\boldsymbol{x}_{m,n,l}-\boldsymbol{x}_{m',n',l'})F^{\mathrm{s},M}_{1,1;m',n',l'},\end{aligned} \tag{65}$$

for $m=1,\ldots,M$, $n=1,\ldots,N$, and $l=1,\ldots,L$. The convolution calculation in the above equation is efficiently carried out using an FFT technique. Here, $F^{\mathrm{p},\Lambda}_{m,n,l}$, $F^{\mathrm{p},\Lambda}_{1,1;m,n,l}$ and $F^{\mathrm{s},\Lambda}_{1,1;m,n,l}$ are related to the finite difference operators in $\mathcal{K}$. We list one as an illustration:

$$\begin{aligned}F^{\mathrm{p},\Lambda}_{m,n,l}=&\overline{\left(\frac{\lambda}{\rho c_{\mathrm{p}}^2}\right)}\left[\overline{\left(\frac{\lambda s^2}{2\mu c_{\mathrm{p}}^2}\right)}r_{k,k;m,n,l}+\frac{1}{(\Delta x_1)^2}(r_{1,1;m-1,n,l}-2r_{1,1;m,n,l}+r_{1,1;m+1,n,l})+\frac{1}{(\Delta x_2)^2}(r_{2,2;m,n-1,l}-2r_{2,2;m,n,l}+r_{2,2;m,n+1,l})\right.\\&+\frac{1}{(\Delta x_3)^2}(r_{3,3;m,n,l-1}-2r_{3,3;m,n,l}+r_{3,3;m,n,l+1})+\frac{1}{4\Delta x_1\Delta x_2}(r_{1,2;m-1,n-1,l}-r_{1,2;m-1,n+1,l}-r_{1,2;m+1,n-1,l}+r_{1,2;m+1,n+1,l})\\&+\frac{1}{4\Delta x_1\Delta x_3}(r_{1,3;m-1,n,l-1}-r_{1,3;m-1,n,l+1}-r_{1,3;m+1,n,l-1}+r_{1,3;m+1,n,l+1})\\&+\frac{1}{4\Delta x_2\Delta x_3}(r_{2,3;m,n-1,l-1}-r_{2,3;m,n+1,l-1}-r_{2,3;m,n-1,l+1}+r_{2,3;m,n+1,l+1})-\overline{\left(\frac{s\rho c_{\mathrm{s}}}{2\mu}\right)}\frac{1}{2\Delta x_1}(r_{0,1;m-1,n,l}-r_{0,1;m+1,n,l})\\&\left.-\overline{\left(\frac{s\rho c_{\mathrm{s}}}{2\mu}\right)}\frac{1}{2\Delta x_2}(r_{0,2;m,n-1,l}-r_{0,2;m,n+1,l})-\overline{\left(\frac{s\rho c_{\mathrm{s}}}{2\mu}\right)}\frac{1}{2\Delta x_3}(r_{0,3;m,n,l-1}-r_{0,3;m,n,l+1})\right],\end{aligned} \tag{66}$$

where $r_{0,k}=r_k$, for $k=1,2,3$. The other components of F have very similar expressions.

4.3.2. The diagonal pre-conditioner

Consider the linear operator $\mathcal{K}$ as a matrix and denote its diagonal matrix as $\mathcal{D}$, we are interested in using $\mathcal{D}^{-1}$ as a pre-conditioner. In other words, instead of solving $\mathcal{K}s_{p,q} = s^{inc}_{p,q}$, we are solving $\mathcal{D}^{-1}\mathcal{K}s_{p,q} = \mathcal{D}^{-1}s^{inc}_{p,q}$. The first component of $\mathcal{D}$ is illustrated below:

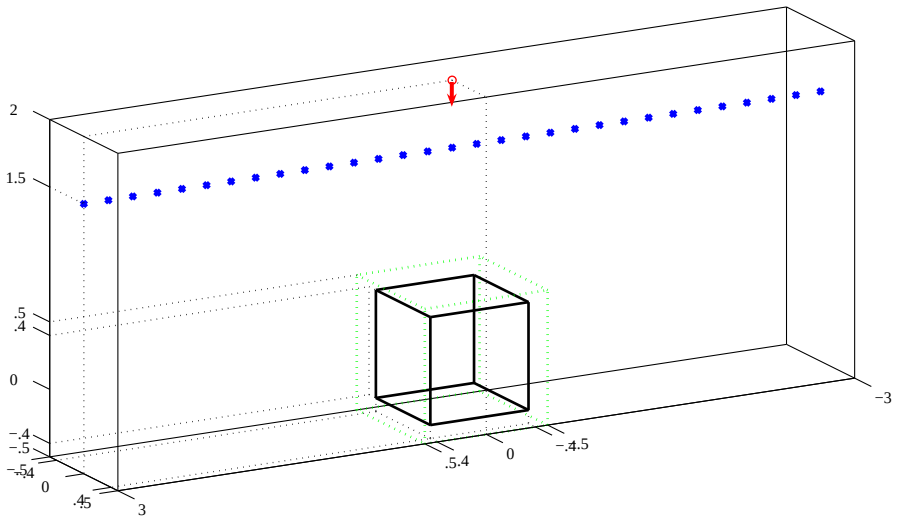

Fig. 2. The configuration for Example I.

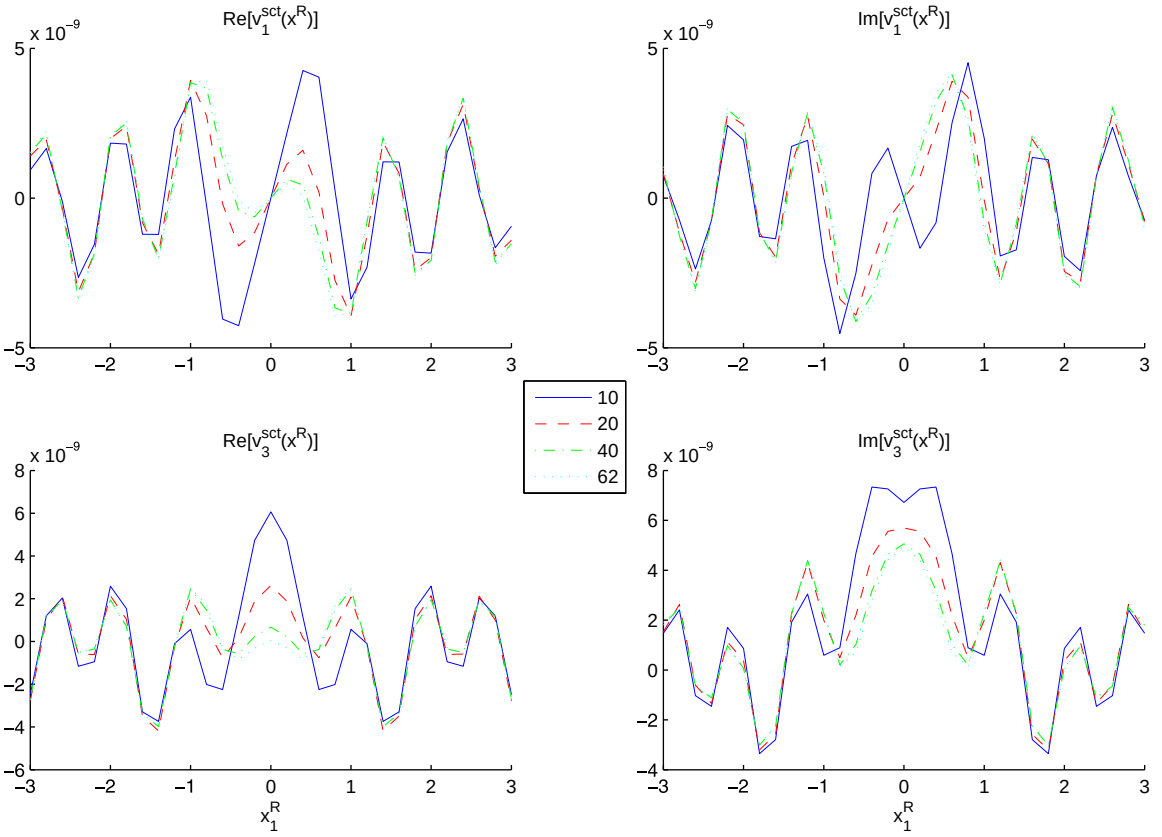

Fig. 3. Convergence test for Example I.

$$\begin{aligned}\mathcal{D}_{1,1;m,n,l} = 1 &+ \frac{\lambda}{\rho c_p^2}\chi^{\Lambda}_{m,n,l} + \frac{\lambda}{\rho c_p^2}\frac{\lambda s^2}{2\mu c_p^2}\Delta V \mathcal{G}^{p}_{0,0,0}\chi^{\Lambda}_{m,n,l} + \frac{\lambda}{\rho c_p^2}\frac{\Delta V}{(\Delta x_1)^2}\chi^{\Lambda}_{m,n,l}\left(\mathcal{G}^{p}_{-1,0,0} - 2\mathcal{G}^{p}_{0,0,0} + \mathcal{G}^{p}_{1,0,0}\right) - \chi^{M}_{m,n,l} - \frac{\lambda}{\rho c_p^2}\chi^{M}_{m,n,l} \\ &- \frac{\lambda}{\rho c_p^2}\frac{\lambda s^2}{2\mu c_p^2}\Delta V \mathcal{G}^{p}_{0,0,0}\chi^{M}_{m,n,l} - 2\frac{\lambda}{\rho c_p^2}\frac{\Delta V}{(\Delta x_1)^2}\chi^{M}_{m,n,l}\left(\mathcal{G}^{p}_{-1,0,0} - 2\mathcal{G}^{p}_{0,0,0} + \mathcal{G}^{p}_{1,0,0}\right) \\ &- 2\frac{\Delta V}{(\Delta x_1)^2}\chi^{M}_{m,n,l}\left(\mathcal{G}^{s}_{-1,0,0} - 2\mathcal{G}^{s}_{0,0,0} + \mathcal{G}^{s}_{1,0,0}\right) - \frac{2c_s^2}{s^2}\frac{\Delta V}{(\Delta x_1)^4}\left[\chi^{M}_{m,n,l}\left(\mathcal{G}^{p}_{-2,0,0} - 2\mathcal{G}^{p}_{-1,0,0} + \mathcal{G}^{p}_{0,0,0}\right)\right. \\ &\left. -2\chi^{M}_{m,n,l}\left(\mathcal{G}^{p}_{-1,0,0} - 2\mathcal{G}^{p}_{0,0,0} + \mathcal{G}^{p}_{1,0,0}\right) + \chi^{M}_{m,n,l}\left(\mathcal{G}^{p}_{0,0,0} - 2\mathcal{G}^{p}_{1,0,0} + \mathcal{G}^{p}_{2,0,0}\right)\right] \\ &+ \frac{2c_s^2}{s^2}\frac{\Delta V}{(\Delta x_1)^4}\left[\chi^{M}_{m,n,l}\left(\mathcal{G}^{s}_{-2,0,0} - 2\mathcal{G}^{s}_{-1,0,0} + \mathcal{G}^{s}_{0,0,0}\right) - 2\chi^{M}_{m,n,l}\left(\mathcal{G}^{s}_{-1,0,0} - 2\mathcal{G}^{s}_{0,0,0} + \mathcal{G}^{s}_{1,0,0}\right)\right. \\ &\left. + \chi^{M}_{m,n,l}\left(\mathcal{G}^{s}_{0,0,0} - 2\mathcal{G}^{s}_{1,0,0} + \mathcal{G}^{s}_{2,0,0}\right)\right]. \end{aligned} \tag{67}$$

The complete explicit expression of $\mathcal{D}$ can be similarly obtained.

4.3.3. The EBA pre-conditioner

We hypothesize that the inverse of a good approximation of the linear operator $\mathcal{K}$ might serve as a better pre-conditioner. Since the Extended Born Approximation (known as EBA) technique has shown to be excellent in other integral equation

Table 1
Convergence test for Example I

N	Relative error in v_1^{sct}	Order	Relative error in v_3^{sct}	Order
10	0.91169		0.91246	
20	0.29922	1.60732	0.35482	1.36263
40	0.07219	2.05135	0.08121	2.12729

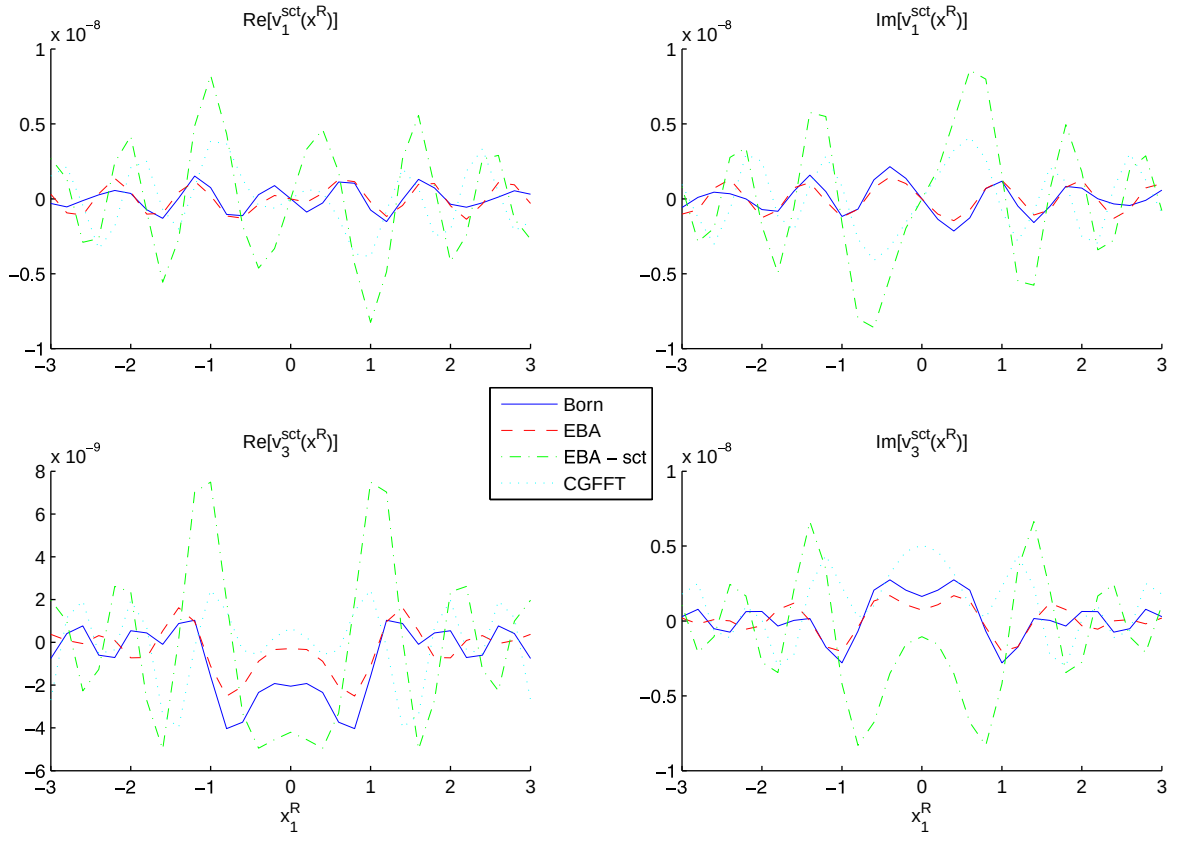

Fig. 4. Scattered field comparison of the four methods at frequency 1.5 kHz for Example I.

problems especially in some electromagnetic applications [1,4]. Therefore, we first investigate its behavior in our problem, and then propose to use it as a pre-conditioner for our iterative solver.

The idea of EBA is to use the following approximation for the internal wavefield inside the integrand of the equations:

$$\tau_{i,j}(\boldsymbol{x}') \approx \tau_{i,j}(\boldsymbol{x}), \quad u_k(\boldsymbol{x}') \approx u_k(\boldsymbol{x}), \quad \boldsymbol{x} \in D, \tag{68}$$

where $\boldsymbol{x}'$ is the integration variable of the integral equation (it also represents the spatial location inside the scatterer) whereas $\boldsymbol{x}$ is the location of the observation point. Hence, we have approximated the internal wavefield by its first term in its Taylor series expansion around the observation variable $\boldsymbol{x}$. Under this localization approximation, Eqs. (32) and (33) are represented by

$$\begin{aligned}\tau^{\mathrm{inc}}_{p,q}(\boldsymbol{x}) &= \tau_{p,q}(\boldsymbol{x}) + \left[s\Lambda \int_D G^{\tau,h}_{p,q,i,i}(\boldsymbol{x}-\boldsymbol{x}')\chi^{\Lambda}(\boldsymbol{x}')\mathrm{d}\boldsymbol{x}'\right]\tau_{k,k}(\boldsymbol{x}) + \left[2sM \int_D G^{\tau,h}_{p,q,i,j}(\boldsymbol{x}-\boldsymbol{x}')\chi^{M}(\boldsymbol{x}')\mathrm{d}\boldsymbol{x}'\right]\tau_{i,j}(\boldsymbol{x}) \\ &\quad - \left[\frac{s}{c_{\mathrm{s}}} \int_D G^{\tau,f}_{p,q,k}(\boldsymbol{x}-\boldsymbol{x}')\chi^{\rho}(\boldsymbol{x}')\mathrm{d}\boldsymbol{x}'\right]u_k(\boldsymbol{x}) \\ &= \tau_{p,q}(\boldsymbol{x}) + E^{\tau,\Lambda}_{p,q}(\boldsymbol{x})\tau_{k,k}(\boldsymbol{x}) + E^{\tau,M}_{p,q,i,j}(\boldsymbol{x})\tau_{i,j}(\boldsymbol{x}) + E^{\tau,\rho}_{p,q,k}(\boldsymbol{x})u_k(\boldsymbol{x}),\end{aligned} \tag{69}$$

$$\begin{aligned}\rho c_{\mathrm{s}} v^{\mathrm{inc}}_r(\boldsymbol{x}) &= u_r(\boldsymbol{x}) - \left[\rho c_{\mathrm{s}} s\Lambda \int_D G^{v,h}_{r,i,i}(\boldsymbol{x}-\boldsymbol{x}')\chi^{\Lambda}(\boldsymbol{x}')\mathrm{d}\boldsymbol{x}'\right]\tau_{k,k}(\boldsymbol{x}) - \left[2\rho c_{\mathrm{s}} sM \int_D G^{v,h}_{r,i,j}(\boldsymbol{x}-\boldsymbol{x}')\chi^{M}(\boldsymbol{x}')\mathrm{d}\boldsymbol{x}'\right]\tau_{i,j}(\boldsymbol{x}) \\ &\quad + \left[s\rho \int_D G^{v,f}_{r,k}(\boldsymbol{x}-\boldsymbol{x}')\chi^{\rho}(\boldsymbol{x}')\mathrm{d}\boldsymbol{x}'\right]u_k(\boldsymbol{x}) \\ &= u_r(\boldsymbol{x}) + E^{u,\Lambda}_{r}(\boldsymbol{x})\tau_{k,k}(\boldsymbol{x}) + E^{u,M}_{r,i,j}(\boldsymbol{x})\tau_{i,j}(\boldsymbol{x}) + E^{u,\rho}_{r,k}(\boldsymbol{x})u_k(\boldsymbol{x}),\end{aligned} \tag{70}$$

where

$$E^{\tau,\Lambda}_{p,q} = \frac{\lambda}{2\mu}\left\{\delta_{p,q}\left[\frac{2c_{\mathrm{s}}^2}{c_{\mathrm{p}}^2}\chi^{\Lambda} + \frac{\lambda s^2}{\rho c_{\mathrm{p}}^4}Y^{\mathrm{p},\Lambda}\right] + \frac{2c_{\mathrm{s}}^2}{c_{\mathrm{p}}^2}\partial_p\partial_q Y^{\mathrm{p},\Lambda}\right\} \tag{71}$$

is a 6×3 matrix,

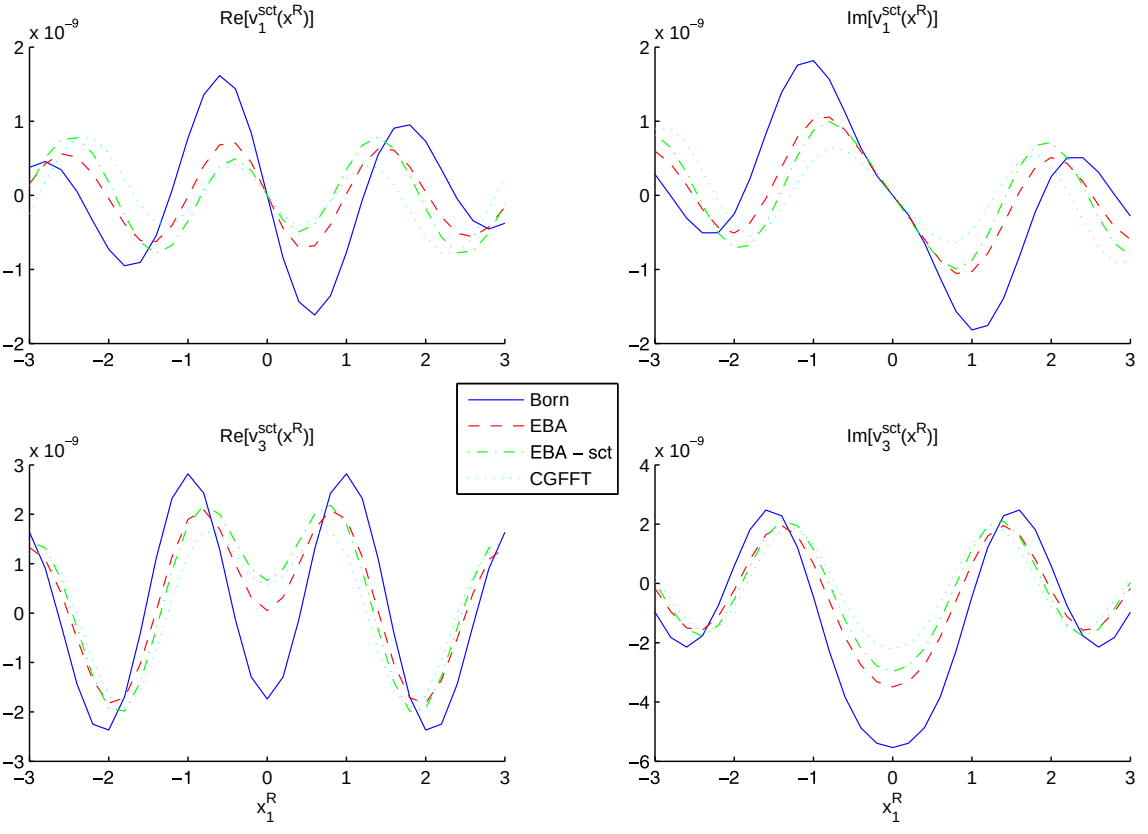

Fig. 5. Scattered field comparison of the four methods at frequency 0.5 kHz for Example I.

$$E^{\tau,M}_{p,q,i,j} = -\frac{\lambda}{2\mu}\left\{\delta_{p,q}\left[\frac{2c_s^2}{c_p^2}\delta_{i,j}\chi^M + \frac{\lambda s^2}{\rho c_p^4}\delta_{i,j}Y^{p,M} + \frac{2c_s^2}{c_p^2}\partial_i\partial_j Y^{p,M}\right] + \frac{2c_s^2}{c_p^2}\delta_{i,j}\partial_p\partial_q Y^{p,M}\right\} - \chi^M(\boldsymbol{x})\delta_{p,i}\delta_{q,j}$$
$$- \left[\delta_{q,i}\partial_p\partial_j Y^{s,M} + \delta_{p,i}\partial_q\partial_j Y^{s,M}\right] - \frac{2c_s^2}{s^2}\partial_p\partial_q\partial_i\partial_j(Y^{p,M} - Y^{s,M}) \tag{72}$$

is a 6×6 matrix,

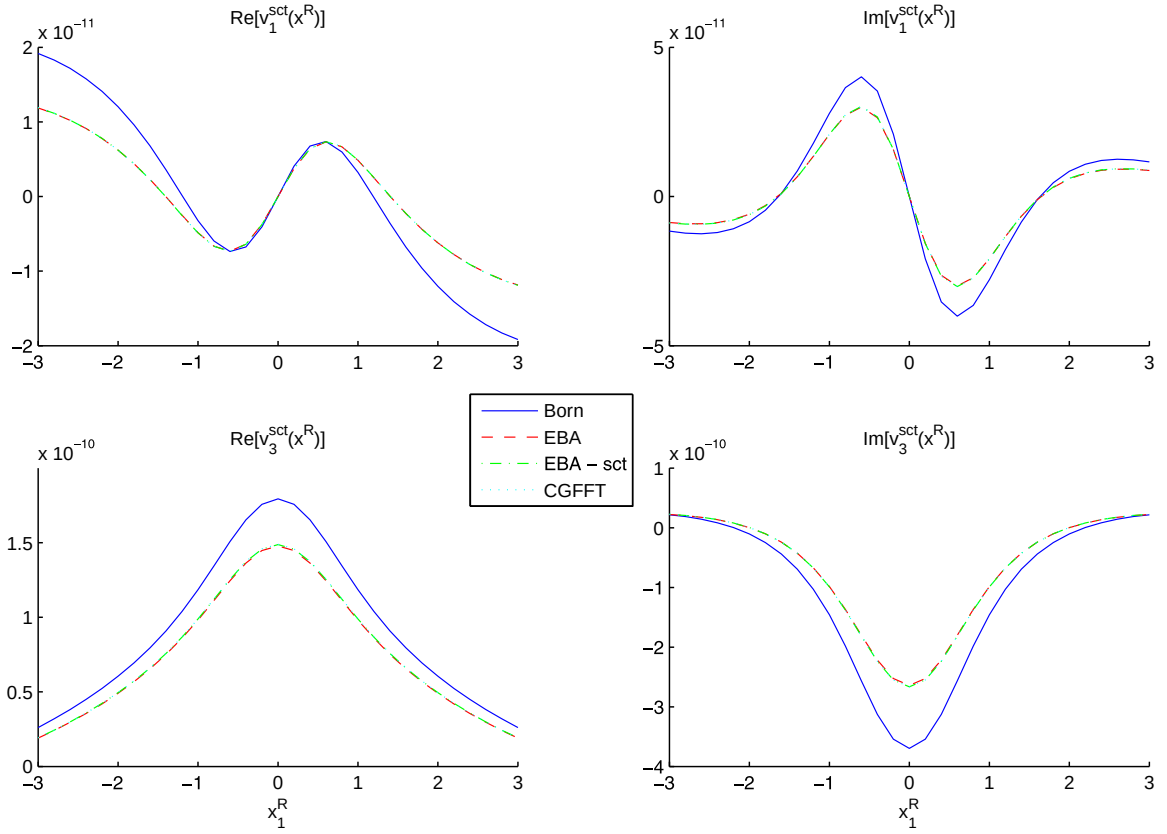

Fig. 6. Scattered field comparison of the four methods at frequency 0.1 kHz for Example I.

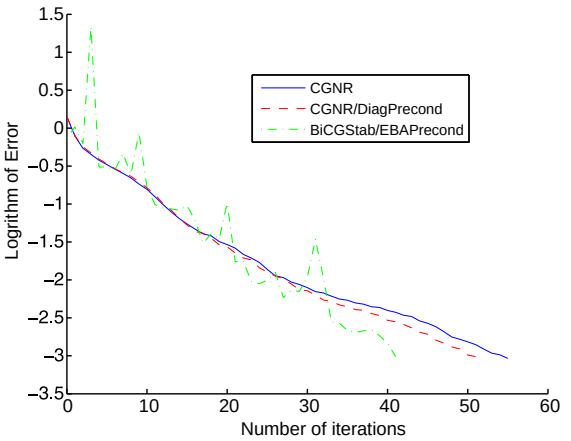

Fig. 7. Scattered field comparison of the three linear solvers at frequency 1.5 kHz for Example I.

$$E^{\tau,\rho}_{p,q,k} = -\frac{\lambda}{\rho c_p^2}\frac{s}{c_s}\delta_{p,q}\partial_k Y^{p,\rho} - \frac{s}{c_s}[\delta_{q,k}\partial_p Y^{s,\rho} + \delta_{p,k}\partial_q Y^{s,\rho}] - \frac{2\mu}{s\rho c_s}\partial_p\partial_q\partial_k(Y^{p,\rho} - Y^{s,\rho}) \tag{73}$$

is a 6×3 matrix,

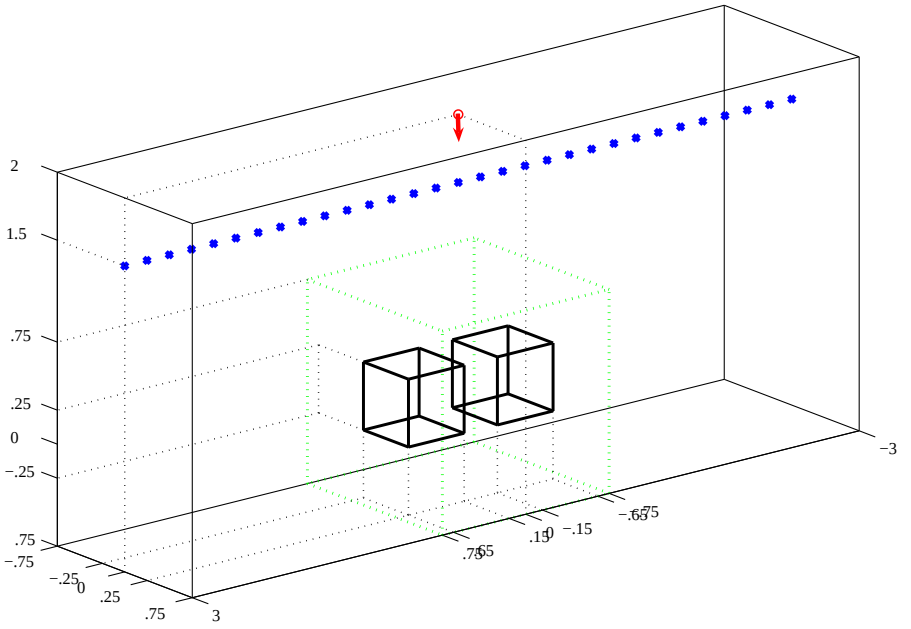

Fig. 8. The configuration for Example II.

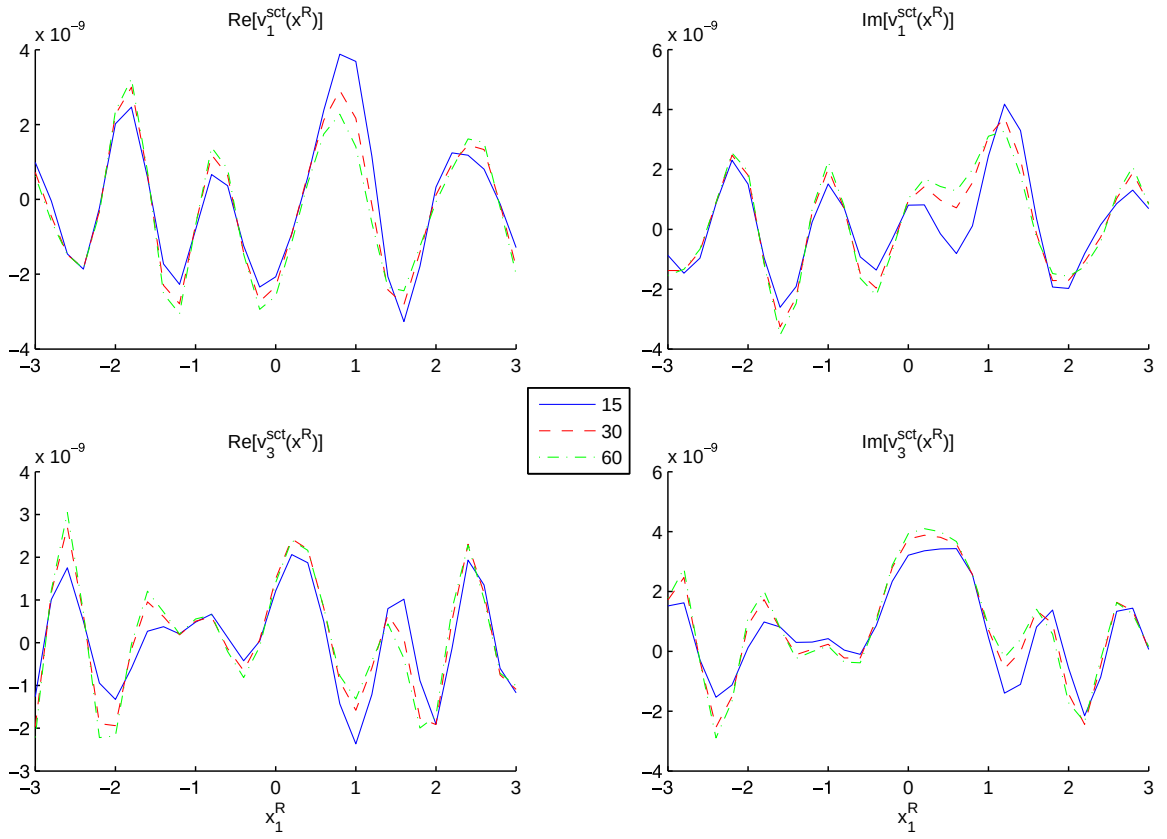

Fig. 9. Convergence test for Example II.

$$E_r^{u,\Lambda}(\boldsymbol{x}) = -\frac{\lambda s c_s}{2\mu c_p^2}\partial_r Y^{p,\Lambda} \tag{74}$$

is a 3×3 matrix,

$$E_{r,ij}^{u,M}(\boldsymbol{x}) = \frac{\lambda s c_s}{2\mu c_p^2}\delta_{ij}\partial_r Y^{p,M} + \frac{s\rho c_s}{\mu}\delta_{rj}\partial_i Y^{s,M} + \frac{c_s}{s}\partial_r\partial_i\partial_j(Y^{p,M} - Y^{s,M}) \tag{75}$$

is a 3×6 matrix, and

$$E_{r,k}^{u,\rho} = \frac{s^2}{c_s^2}\delta_{r,k}Y^{s,\rho} + \partial_r\partial_k(Y^{p,\rho} - Y^{s,\rho}), \tag{76}$$

is a 3×3 matrix. Here, we define

$$Y^{\gamma,\beta}(\boldsymbol{x}) = \int_D G^{\gamma}(\boldsymbol{x} - \boldsymbol{x}')\chi^{\beta}(\boldsymbol{x}')\mathrm{d}\boldsymbol{x}', \tag{77}$$

where $\gamma \in \{p, s\}$ and $\beta \in \{\Lambda, M, \rho\}$. Explicitly, Eqs. (69) and (70) can be written as follows

$$\left[\tau_{1,1}^{inc}, \tau_{2,2}^{inc}, \tau_{3,3}^{inc}, \tau_{1,2}^{inc}, \tau_{1,3}^{inc}, \tau_{2,3}^{inc}, u_1^{inc}, u_2^{inc}, u_3^{inc}\right]^T = \Gamma \cdot [\tau_{1,1}, \tau_{2,2}(\boldsymbol{x}), \tau_{3,3}, \tau_{1,2}, \tau_{1,3}, \tau_{2,3}, u_1, u_2, u_3]^T, \tag{78}$$

Table 2
Convergence test for Example II

N	Relative error in v_1^{sct}	Order	Relative error in v_3^{sct}	Order
15	0.44879		0.39363	
30	0.14392	1.64069	0.11149	1.81990

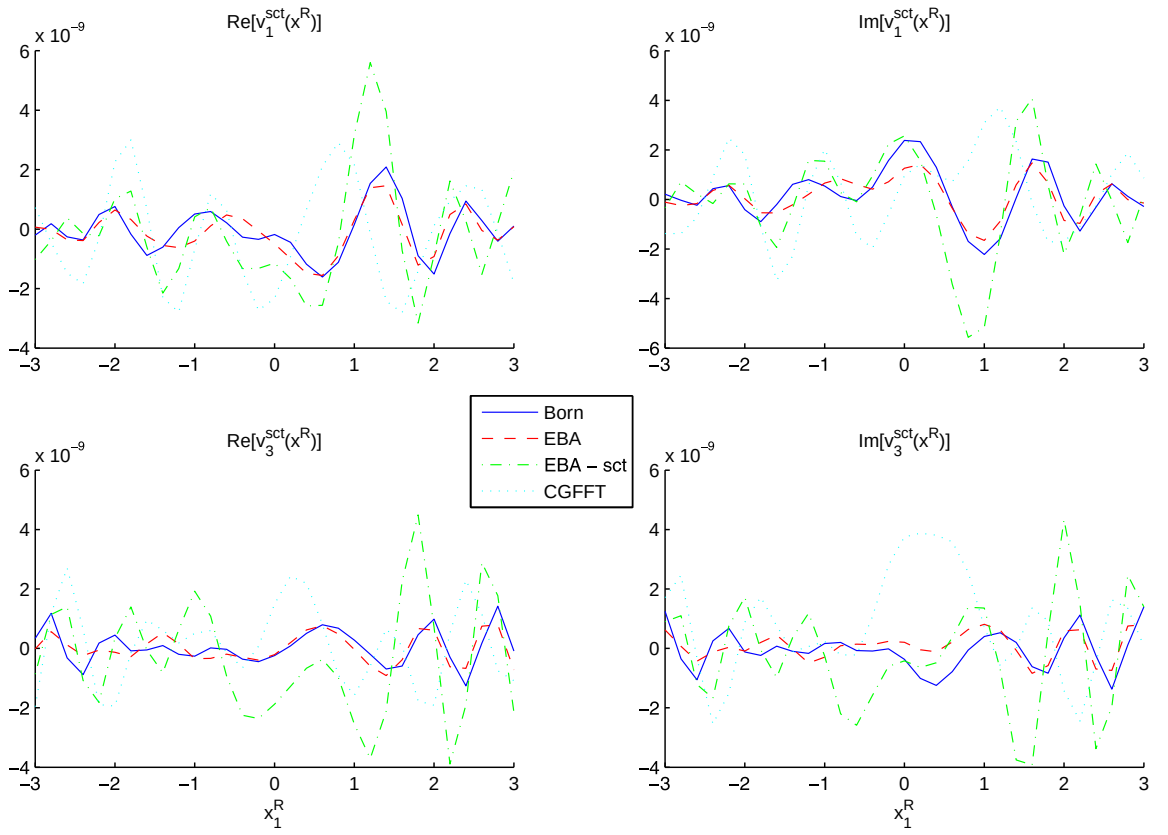

Fig. 10. Scattered field comparison of the four methods at frequency 1.5 kHz for Example II.

where T is the transpose notation, and $\Gamma = \Gamma(\boldsymbol{x})$ is a 9×9 matrix given by

$$\Gamma = \mathbf{I}_{9\times 9} + \begin{bmatrix} E^{\tau,\Lambda} & \mathbf{0}_{6\times 6} \\ E^{u,\Lambda} & \mathbf{0}_{3\times 6} \end{bmatrix} + \begin{bmatrix} E^{\tau,M} & E^{\tau,\rho} \\ E^{u,M} & E^{u,\rho} \end{bmatrix}. \tag{79}$$

Therefore, following the same discretization procedure, we are able to implement the EBA operator Γ, and use its inverse operator as a pre-conditioner. In other words, instead of solving $\mathcal{K}s_{p,q} = s^{inc}_{p,q}$, we are solving $\Gamma^{-1}\mathcal{K}s_{p,q} = \Gamma^{-1}s^{inc}_{p,q}$.

4.4. Discretized integral representation

Using the same discretization procedure, the scattered field of particle velocity in Eq. (47) can be represented as follows:

$$\begin{aligned} v_r^{sct}(x_1^R, x_2^R, x_3^R) = {} & \frac{\lambda}{2\mu}\frac{s}{\rho c_p^2}\Delta V \sum_{m=1}^{M}\sum_{n=1}^{N}\sum_{l=1}^{L} \partial_r G^p(\boldsymbol{x}^R - \boldsymbol{x}_{m,n,l})\chi^{\Lambda}_{m,n,l}\tau_{k,k;m,n,l} - \frac{\lambda}{2\mu}\frac{s}{\rho c_p^2}\Delta V \sum_{m=1}^{M}\sum_{n=1}^{N}\sum_{l=1}^{L} \partial_r G^p(\boldsymbol{x}^R - \boldsymbol{x}_{m,n,l})\chi^{M}_{m,n,l}\tau_{k,k;m,n,l} \\ & - \frac{1}{\rho s}\Delta V \sum_{m=1}^{M}\sum_{n=1}^{N}\sum_{l=1}^{L} \partial_r\partial_i\partial_j G^p(\boldsymbol{x}^R - \boldsymbol{x}_{m,n,l})\chi^{M}_{m,n,l}\tau_{i,j;m,n,l} + \frac{1}{\rho s}\Delta V \sum_{m=1}^{M}\sum_{n=1}^{N}\sum_{l=1}^{L} \partial_r\partial_i\partial_j G^s(\boldsymbol{x}^R - \boldsymbol{x}_{m,n,l})\chi^{M}_{m,n,l}\tau_{i,j;m,n,l} \\ & - \frac{s}{\rho c_s^2}\Delta V \sum_{m=1}^{M}\sum_{n=1}^{N}\sum_{l=1}^{L} \partial_j G^s(\boldsymbol{x}^R - \boldsymbol{x}_{m,n,l})\chi^{M}_{m,n,l}\tau_{r,j;m,n,l} - \frac{s^2}{\rho c_s^3}\Delta V \sum_{m=1}^{M}\sum_{n=1}^{N}\sum_{l=1}^{L} G^s(\boldsymbol{x}^R - \boldsymbol{x}_{m,n,l})\chi^{\rho}_{m,n,l}u_{r;m,n,l} \\ & - \frac{1}{\rho c_s}\Delta V \sum_{m=1}^{M}\sum_{n=1}^{N}\sum_{l=1}^{L} \partial_r\partial_k G^p(\boldsymbol{x}^R - \boldsymbol{x}_{m,n,l})\chi^{\rho}_{m,n,l}u_{k;m,n,l} + \frac{1}{\rho c_s}\Delta V \sum_{m=1}^{M}\sum_{n=1}^{N}\sum_{l=1}^{L} \partial_r\partial_k G^s(\boldsymbol{x}^R - \boldsymbol{x}_{m,n,l})\chi^{\rho}_{m,n,l}u_{k;m,n,l}, \end{aligned} \tag{80}$$

where x_1^R, x_2^R and x_3^R are the receiver spatial positions located outside the computational domain D. Hence, all the spatial differentiation operators working on the scalar Green functions are calculated in closed forms.

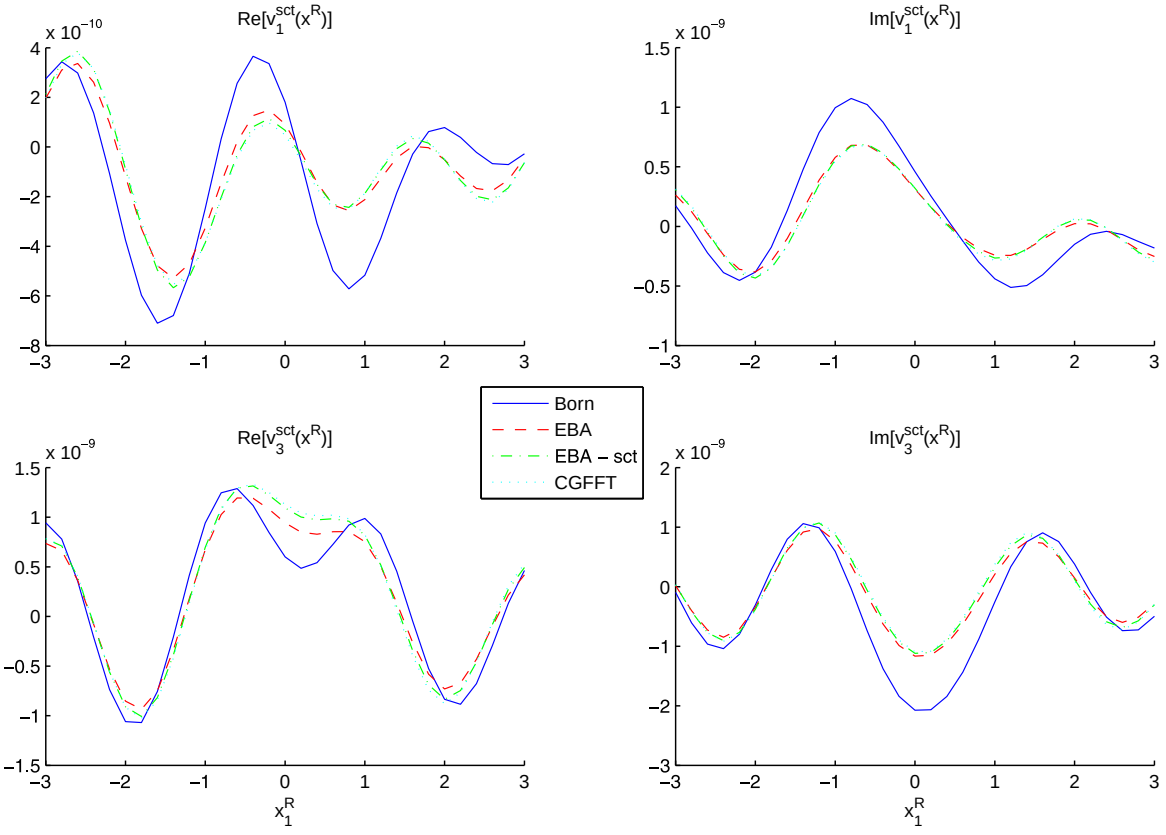

Fig. 11. Scattered field comparison of the four methods at frequency 0.5 kHz for Example II.

5. Numerical results

Throughout our numerical tests in this section, the background material always has a compressional speed of 1500 m/s and a shear speed of 1000 m/s. The mass density is 2000 kg/m^3. The point excitation force employed is directed in the negative vertical x_3-direction located at (0,0,2) m. There are 30 receivers equally arranged along the line from $(-3.0, 0, 1.5)$ m to (3.0, 0, 1.5) m. The frequency of operation is 1.5 kHz.

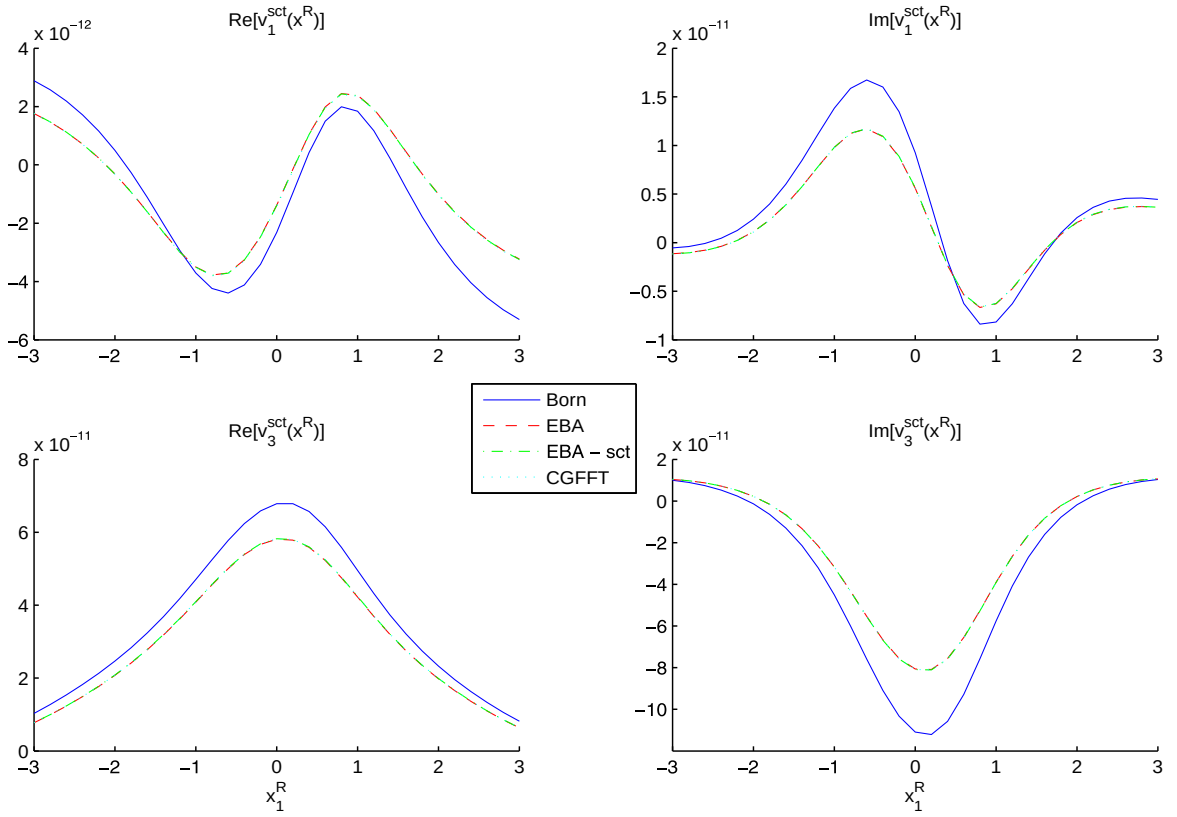

Fig. 12. Scattered field comparison of the four methods at frequency 0.1 kHz for Example II.

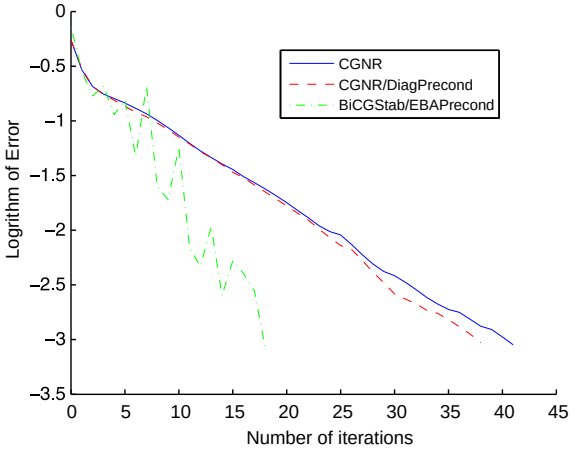

Fig. 13. Scattered field comparison of the three linear solvers at frequency 1.5 kHz for Example II.

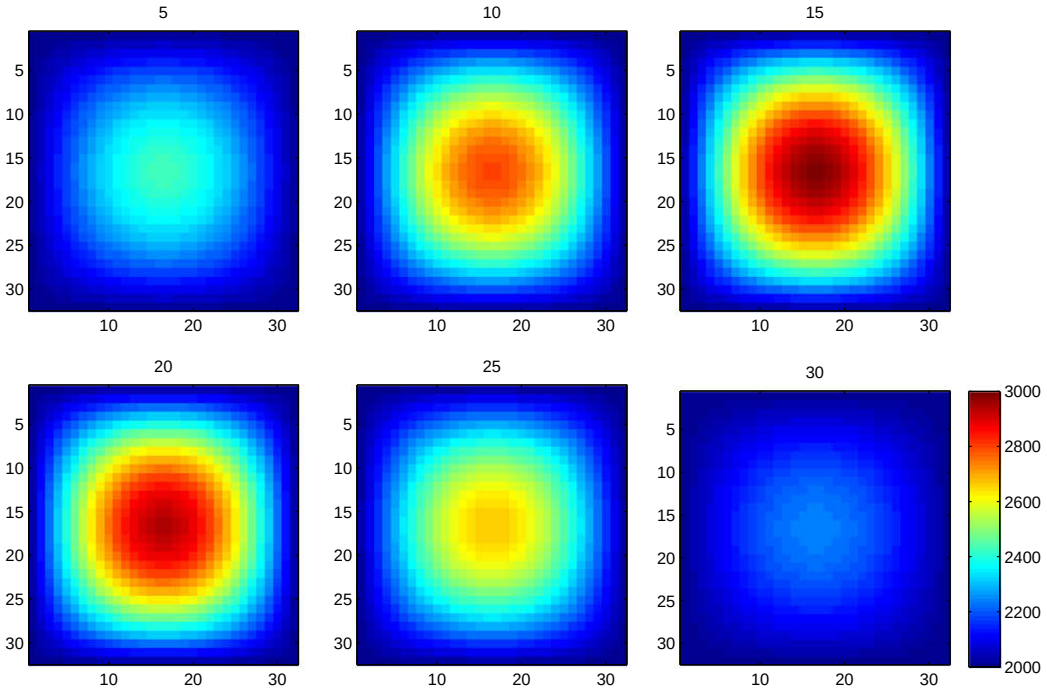

Fig. 14. The horizontal slice images for Example III.

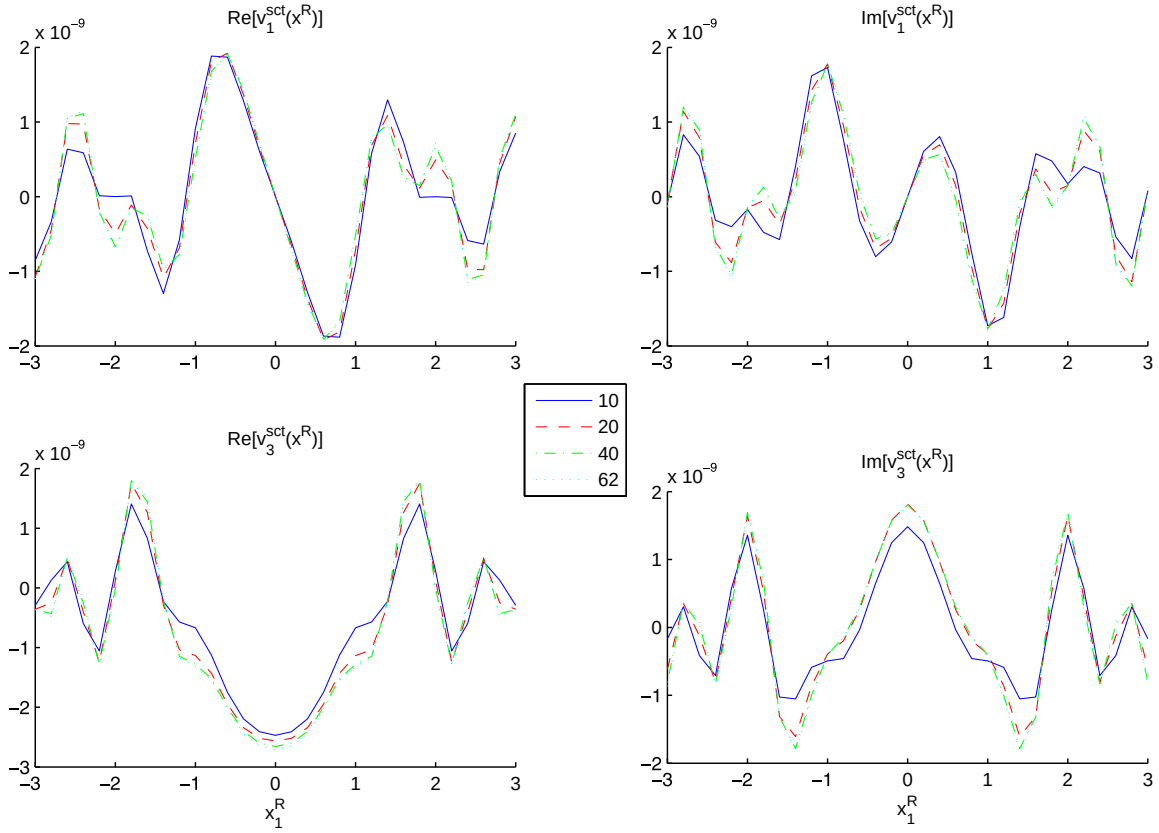

Fig. 15. Consistency test: Example III.

5.1. Example I

The first model we consider is an object with dimension 0.8 m × 0.8 m × 0.8 m as shown in Fig. 2. The object has a mass density of 3000 kg/m^3, a compressional speed of 3000 m/s and a shear speed of 2000 m/s. The computational domain D is of dimension 1.0 m × 1.0 m × 1.0 m, and its center is located at (0,0,0) m.

First, we perform a convergence test as we refine the grids. Fig. 3 shows the scattered particle velocities at the receivers when the number of computational points along each axis is 10, 20, 40 and 62, respectively. The curves show that the scattered particle velocities convergence as we refine the grids. Table 1 shows the convergence history of the test, where the benchmark fields are calculated from the grids which have 62 computational points along each axis. Therefore, we would claim that this algorithm is second order in terms of convergence rate.

To show that EBA is a good approximation to the integral equation operator, we compare the results among the following three methods: normalized integral equation of total field, extended Born approximation to the normalized integral equation of total field, and extended Born approximation to the normalized integral equation of scattered field. Fig. 4 shows the comparison at frequency 1.5 kHz, where there are 40 computational points along each axis. Fig. 5 shows the comparison at frequency 0.5 kHz, where there are 20 computational points along each axis. Fig. 6 shows the comparison with frequency 0.1 kHz, where there are 20 computational points along each axis.

As shown in these figures, the EBA approximations are getting better as the frequency of operation decreases. We therefore show in Fig. 7 the comparison of the three linear system solvers: CGNR, CGNR with diagonal matrix pre-conditioner, BiCGStab with EBA pre-conditioner. The diagonal matrix pre-conditioner helps to improve the condition of the matrix, however, EBA pre-conditioner works better.

Table 3
Convergence test for Example III

N	Relative error in v_1^{sct}	Order	Relative error in v_3^{sct}	Order
10	0.39310		0.31772	
20	0.15304	1.36097	0.10925	1.54012
40	0.03404	2.16867	0.02797	1.96522

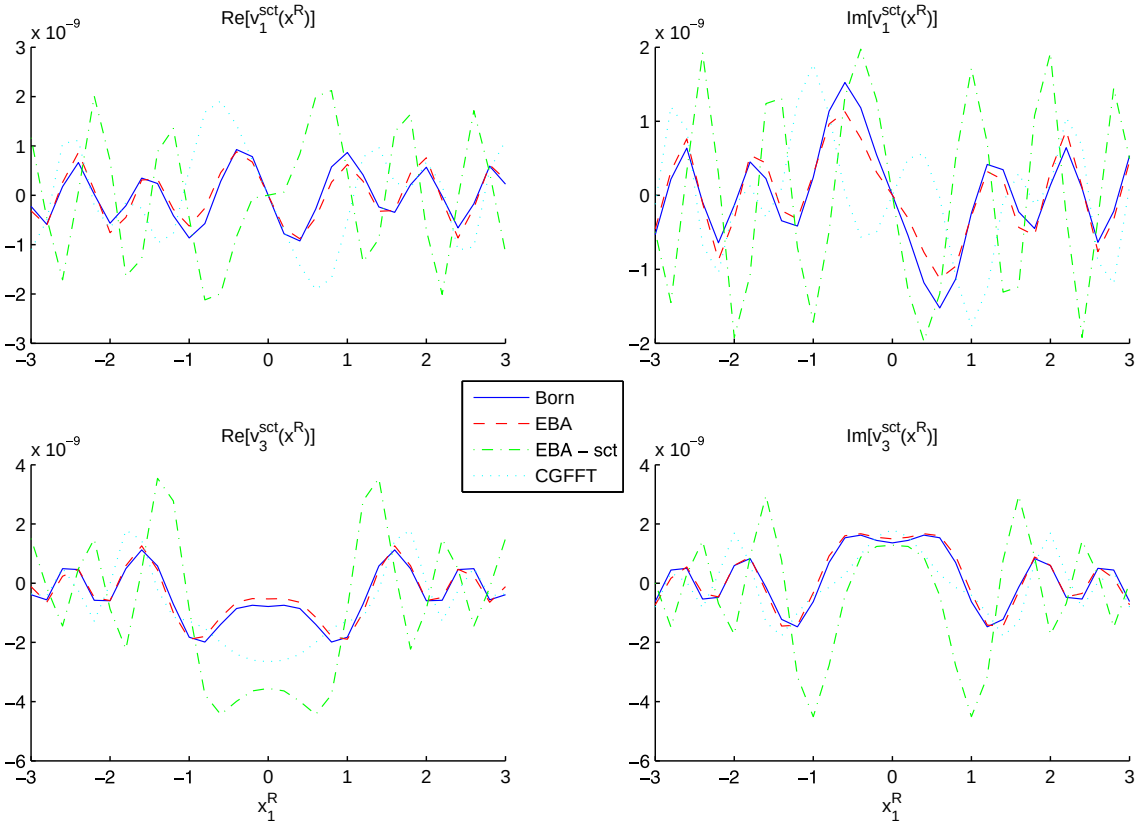

Fig. 16. Scattered field comparison of the four methods at frequency 1.5 kHz for Example III.

5.2. Example II

The second model we consider has two objects, which have the same dimensions of 0.5 m × 0.5 m × 0.5 m, as shown in Fig. 8. The object on the left has a mass density of 3000 kg/m^3, a compressional speed of 3000 m/s and a shear speed of 1000 m/s, while the object on the right has a density of 3000 kg/m^3, a compressional speed of 1500 m/s and a shear speed of 2000 m/s. The computational domain is a cube of dimension 1.5 m × 1.5 m × 1.5 m centered at (0,0,0) m.

We first perform a convergence test shown in Fig. 9 for the scattered particle velocities measured at the receivers for an increasing number of computational points along each axis: 15, 30 and 60. The curves show that the scattered particle velocities convergence as the grids are refined. Table 2 shows the convergence history of the test, where the benchmark fields are calculated from the grids which have 60 computational points along each axis. Again, we claim that this algorithm is second order in terms of convergence rate.

We compare the results of the following four methods: normalized integral equation of total field, Born approximation for the normalized integral equation of total field, extended Born approximation for the normalized integral equation of total field, and extended Born approximation for the normalized integral equation of scattered field. Fig. 10 shows the comparison at frequency 1.5 kHz, where there are 30 computational points along each axis. Fig. 11 shows the comparison at frequency 0.5 kHz, where there are 30 computational points along each axis. Fig. 12 shows the comparison at frequency 0.1 kHz, where there are 30 computational points along each axis.

Once again, we can conclude from these figures that the EBA approximations are getting better when the frequency of operation decreases. Fig. 13 shows the comparison of the three linear system solvers as before. The diagonal matrix pre-conditioner works better while the EBA pre-conditioner are the best.

5.3. Example III

Unlike the first two models where the objects have constant material properties, the third model we tested has an object which is inhomogeneous in itself. The geometry of the third model is the same as the first model, as shown in Fig. 2, however, the material properties inside the object are given as follows:

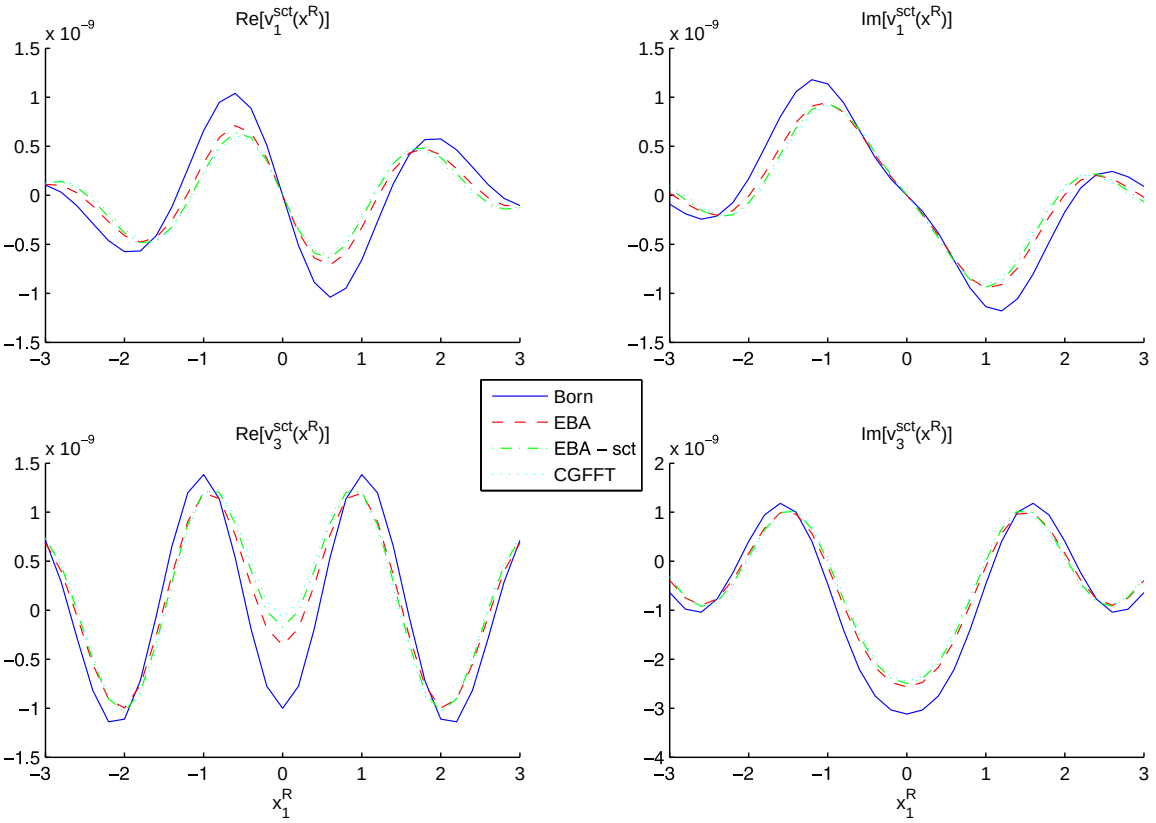

Fig. 17. Scattered field comparison of the four methods at frequency 0.5 kHz for Example III.

$$
\begin{aligned}
c_p &= 1500 + 1500 \sin\left[\frac{(x+0.4)\pi}{0.8}\right] \sin\left[\frac{(y+0.4)\pi}{0.8}\right] \sin\left[\frac{(z+0.4)\pi}{0.8}\right], \\
c_s &= 1000 + 1000 \sin\left[\frac{(x+0.4)\pi}{0.8}\right] \sin\left[\frac{(y+0.4)\pi}{0.8}\right] \sin\left[\frac{(z+0.4)\pi}{0.8}\right], \\
\rho &= 2000 + 1000 \sin\left[\frac{(x+0.4)\pi}{0.8}\right] \sin\left[\frac{(y+0.4)\pi}{0.8}\right] \sin\left[\frac{(z+0.4)\pi}{0.8}\right].
\end{aligned} \tag{81}
$$

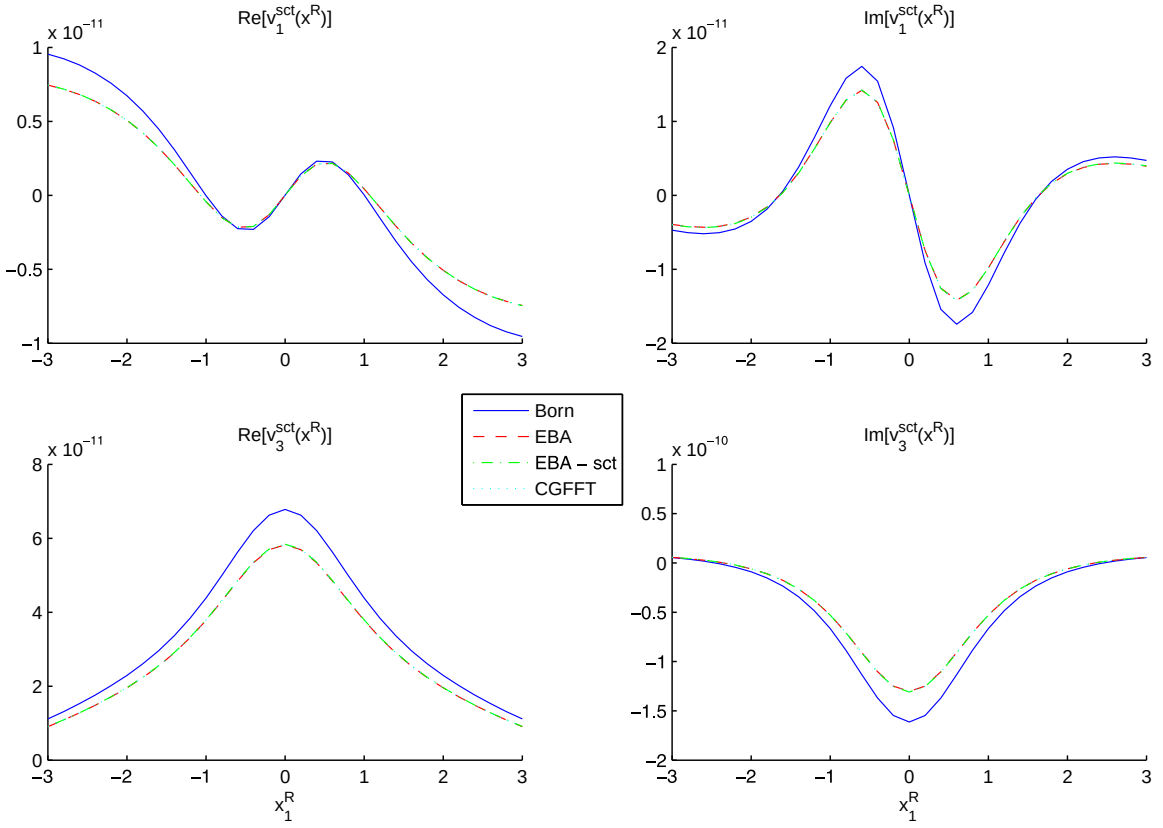

Fig. 18. Scattered field comparison of the four methods at frequency 0.1 kHz for Example III.

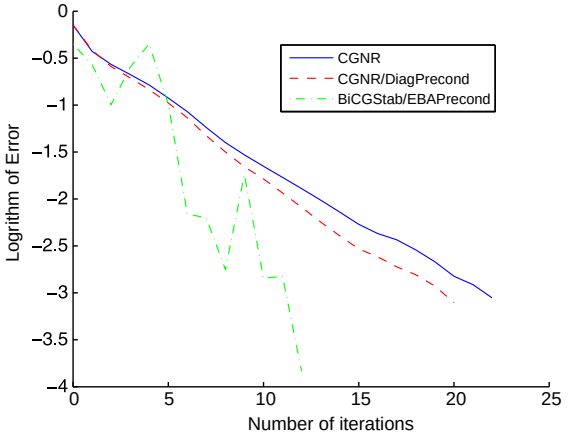

Fig. 19. Scattered field comparison of the three linear solvers at frequency 1.5 kHz for Example III.

Fig. 14 shows some horizontal image slices of the density of the object. The slices for c_p and c_s are similar.

We again perform a convergence test first. Fig. 15 shows the scattered particle velocities at the receivers when the number of computational points along each axis is 10, 20, 40 and 62. The curves show that the scattered particle velocities convergence as the grids are refined. Table 3 shows the convergence history of the test, where the benchmark fields are calculated from the grids which have 62 computational points along each axis. Therefore, we would claim that this algorithm is second order in terms of convergence rate.

We then compare the results of the following four methods: normalized integral equation of total field, Born approximation for the normalized integral equation of total field, extended Born approximation for the normalized integral equation of total field, and extended Born approximation for the normalized integral equation of the scattered field. Fig. 16 shows the comparison between these methods at frequency 1.5 kHz, where there are 40 computational points along each axis. Fig. 17 shows the comparison at frequency 0.5 kHz, where there are 20 computational points along each axis. Fig. 18 shows the comparison at frequency 0.1 kHz, where there are 20 computational points along each axis.

Once again, we can conclude from the above figures that the EBA approximations are getting better when the frequency of operation decreases. Again, Fig. 19 shows the comparison among the three linear system solvers as before. The diagonal matrix pre-conditioner works well while the EBA pre-conditioners are the best.

6. Conclusions

In this paper we introduced a Conjugate Gradient Fast Fourier Transform (CG-FFT) method for the numerical solution of a Lippman–Schwinger integral equation formulation of three-dimensional elastic scattering problems. To alleviate conditioning difficulties that may arise from differentiation of unknown fields within the formulation, as in classical approaches that treat the displacements as the primary dependent variables, we resort here to a representation in terms of stress fields and particle velocities. For the resulting equations we derive and implement a numerical procedure that relies on accurate quadrature formulas and efficient FFT evaluations of the iterative solution of the discretized problem. The convergence of the CG iterative scheme is further improved through the introduction of suitable pre-conditioners, most notably those based on the Extended Born Approximation. A variety of numerical examples are presented that confirm the accuracy and efficiency of the proposed methodology. These features suggest that the present numerical scheme could provide the basis for efficient inversion procedures [2,11] that require the repeated application of forward scattering simulators, the development of which is left for future work.

References

[1] A. Abubakar, P.M. van den Berg, Three-dimensional inverse scattering applied to cross-well induction sensors, IEEE Transactions on Geoscience and Remote Sensing 38 (4) (2000) 1669–1681.
[2] A. Abubakar, Three-Dimensional Nonlinear Inversion of Electrical Conductivity, Ph.D. Thesis, Delft University Press, Delft, 2000 (Chapter 3).
[3] A. Abubakar, P.M. van den Berg, Iterative forward and inverse algorithms based on domain integral equations for three-dimensional electric and magnetic objects, Journal of Computational Physics 195 (2004) 236–262.
[4] A. Abubakar, T.M. Habashy, A green function formulation of the extended born approximation for three-dimensional electromagnetic modelling, Wave Motion 41 (3) (2005) 211–227.
[5] E.J. Aymé-Bellegarda, T.M. Habashy, J.R. Bellegarda, Automatic recognition of multidimensional objects buried in layered elastic background media, Optical Engineering 31 (12) (1992) 2572–2579.
[6] E.J. Aymé-Bellegarda, T.M. Habashy, Ultrasonic inverse scattering of multidimensional objects buried in multilayered elastic background, IEEE Transactions on Ultrasonics, Ferroelectrics, and Frequency Control 39 (1) (1992) 11–18.
[7] E.J. Aymé-Bellegarda, T.M. Habashy, On multidimensional ultrasonic scattering in an inhomogeneous elastic background, Journal of Acoustical Society of America 91 (6) (1992) 3104–3115.
[8] T.M. Habashy, R.W. Groom, B. Spies, Beyond the Born and Rytov approximations: a nonlinear approach to electromagnetic scattering, Journal of Geophysics Research 98 (1993) 1759–1775.
[9] A.T. de Hoop, The Handbook of Radiation and Scattering of Waves, Academic Press, Delft, 1995 (Chapter 10).
[10] G. Pelekanos, R.E. Kleinman, P.M. van den Berg, A weak form of the conjugate Gradient FFT method for two-dimensional elastodynamics, Journal of Computational Physics 160 (2000) 597–611.
[11] G. Pelekanos, A. Abubakar, P.M. van den Berg, Contrast source inversion methods in elastodynamics, Journal of Acoustical Society of America 114 (5) (2003) 2825–2834.
[12] P. Zwamborn, P.M. van den Berg, The three dimensional weak form of the conjugate gradient FFT method for solving scattering problems, IEEE Transactions on Microwave Theory and Techniques 40 (9) (1992) 1757–1766.
[13] K. Aki, P.G. Richards, Quantitative Seismology: Theory and Methods, Freeman, San Francisco, 1998.
[14] W.M. Ewing, W.S. Jardetzky, F. Press, Elastic Waves in Layered Media, McGRAW-HILL Book Company, 1957 (Chapter 1).
[15] B.B. Guzina, S.N. Fata, M. Bonnet, On the stress-wave imaging of cavities in a semi-infinite solid, International Journal of Solids and Structures 40 (6) (2003) 1505–1523.
[16] B.B. Guzina, M. Bonnet, Topological derivative for the inverse scattering of elastic waves, Quarterly Journal of Mechanics and Applied Mathematics 57 (2) (2004) 161–179.
[17] I. Harari, A survey of finite element methods for time-harmonic acoustics, Computer Methods in Applied Mechanics and Engineering 195 (2006) 1594–1607.
[18] M. Fatemi, J.F. Greenleaf, Vibro-acoustography: an imaging modality based on ultrasound-stimulated acoustic emission, Proceedings of the National Academy of Sciences 96 (1999) 6603–6608.
[19] J.T. Fokkema, P.M. van den Berg, Seismic Applications of Acoustic Reciprocity, Elsevier, Amsterdam, 1993 (Chapter 2).
[20] A. Greenbaum, Iterative Methods for Solving Linear Systems, SIAM, Philadelphia, 1997 (Chapter 8).
[21] Y. Liu, F.J. Rizzo, Hypersingular boundary integral equations for radiation and scattering of elastic waves in three dimensions, Computer Methods in Applied Mechanics and Engineering 107 (1-2) (1993) 131–144.

[22] Y. Liu, F.J. Rizzo, Scattering of elastic waves from thin shapes in three dimensions using the composite boundary integral equation formulation, Journal of the Acoustical Society of America 102 (2) (1997) 926–932.
[23] S.E. Minkoff, Spatial parallelism of a 3D finite difference velocity-stress elastic wave propagation code, Journal on Scientific Computing 24 (1) (2002) 1–19.
[24] M. Nieto-Vesperinas, Scattering and Diffraction in Physical Optics, Wiley, New York, 1991.
[25] W.H. Press, S.A. Teukolsky, W.T. Vetterling, B.P. Flannery, Numerical Recipes in FORTRAN – the art of scientific computing, Cambridge University Press, Cambridge, 1992.
[26] J.H. Richmond, Scattering by a dielectric cylinder of arbitary cross section shape, IEEE Transactions on Antennas and Propagation 13 (1965) 334–341.
[27] R. Schirrer, R. Lenke, J. Boudouaz, Study of mechanical damage in rubber-toughened poly(methyl methacrylate) by single and multiple scattering of light, Polymer Engineering and Science 37 (10) (1997) 1748–1760.
[28] R. Snieder, General theory of elastic wave scattering, Scattering and Inverse Scattering in Pure and Applied Science, Academic Press, San Diego, 2002. 528–542.
[29] G. Vainikko, Multedimensional Weakly Singular Integral Equations, Springer-Verlag, New York, 1993.
[30] H.A. Van Der Vorst, Bi–CGStab: a fast and smoothly converging variant of Bi–CG for the solution of nonsymmetric linear systems, SIAM Journal on Scientific and Statistical Computing 13 (2) (1992) 631–644.
[31] J. Virmont, G. Ledanois, New Aspects of Electromagnetic and Acoustic Wave Diffusion, Optical Medical Diagnostics and Imaging, Springer-Verlag, Telos, 1998.
[32] Y. Yazicioglu, T.J. Royston, T. Spohnholtz, B. Martin, F. Loth, H.S. Bassiouny, Acoustic radiation from a fluid-filled, subsurface vascular tube with internal turbulent flow due to a constriction, Journal of the Acoustical Society of America 118 (2) (2002) 1193–1209.
[33] Z.Q. Zhang, Q.H. Liu, Three-dimensional weak-form conjugate- and biconjugate-gradient FFT methods for volume integral equations, Microwave and Optical Technology Letters 29 (5) (2001) 350–356.